Satellite Dynamics in Dark Matter Halos

by

Farbod Kamiab

A thesis
presented to the University of Waterloo
in fulfillment of the
thesis requirement for the degree of
Master of Science
in
Physics

Waterloo, Ontario, Canada, 2010

I hereby declare that I am the sole author of this thesis. This is a true copy of the thesis, including any required final revisions, as accepted by my examiners.

I understand that my thesis may be made electronically available to the public.

Abstract

I have used an analytic model of tidal interactions to predict the evolution of a substructure in a static dark matter halo. Given the initial conditions of the satellite and background halo, the model predicts with high accuracy the mass loss of the satellite and also its density evolution. The main phenomena taken into account in the model are tidal truncation at the tidal radius of the satellite and heating due to tidal shocks at the pericenter of its orbit. To calibrate and test the model, it has been compared with numerical simulations of a satellite orbiting in a static dark matter halo. The model predicts a set of tidal radii for the satellite in different stages of its evolution. The mass of the satellite is accurately calculated at each stage by truncating an NFW (Navarro, Frenk and White) profile at the tidal radius. The mass lost beyond the tidal limit is scaled by half the instantaneous orbital period of the satellite. The model can also be used to predict analytically the new density profile of the satellite. This new profile is given by a modification of the NFW density profile as a function of radius. The tidal radius is the only parameter going into this modification. The effect of numerical relaxation has been studied and quantified by performing the same simulations in lower resolutions. I find that substructures with less than 1000 particles are artificially relaxed and this process affects their mass loss and results in their premature disruptions. This underlines the utility of an analytic model predicting the evolution of substructures in minor mergers.

Acknowledgements

I owe my deepest gratitude to my supervisor, Dr. James Taylor, whose expertise, understanding and patience added considerably to my graduate experience. Throughout my thesis-writing period, he provided encouragement and sound advice. This would have been impossible without him.

I would like to thank the other members of my committee, Dr. Michael Balogh (my co-supervisor) and Dr. Brian McNamara for the assistance they provided throughout my studies. I am also grateful to Dr. Kostadinka Bizheva for taking time out from her busy schedule to read my thesis.

I would like to acknowledge the help of Dr. Niayesh Afshordi for regularly and patiently answering my questions. I am indebted to my friends Chad Greene, Ting Lu, Sean McGee and Amir Baserinia for their great ideas and valuable help in preparing this thesis. A special thanks goes to my affectionate friend Mina Rohanizadegan.

Lastly, and most importantly, I wish to thank my parents, Farahnaz Malekyazdi and Kavé Kamiab, for their love and support. To them I dedicate this thesis.

To Nana & Babi

Contents

List of Figures

List of Tables

Chapter 1

Introduction

Thousands of years ago, when humans looked at the night sky, they saw bright dots and described them as shining candles rotating around us. We thought we were special, at the center of the universe. It was only about 500 years ago, that Copernicus and Galileo proved us wrong. The Copernican revolution dethroned us from our privileged position and placed the Earth rotating around the Sun, a star among many others. As we could only see a few thousand stars at most with our unaided eyes, our picture of the universe was dramatically changed in the 20th century with the advent of powerful telescopes and computers. Figure 1.1 illustrates one of the deepest pictures of the universe taken by the Hubble Telescope. Each spot is a galaxy, consisting of billions of stars. The study of galaxies has led to major advances in the field of cosmology. For instance Edwin Hubble observed the recession of galaxies in 1929 and this observation became the empirical basis of the expanding universe paradigm. This gave birth to the Big Bang model which was later confirmed by additional evidence such as the Cosmic Microwave Background, the first free photons traveling to us from the early universe.

From Big Bang theory and also from observations of the early universe, we can construct a cosmological model. Such a model specifies the content of the universe and the initial conditions (small perturbations in the density and velocity field of matter) which coupled with a growth mechanism give rise to existing structures in the universe such as

Figure 1.1: Hubble Ultra Deep Field (HUDF), NASA and the European Space Agency. Equivalent sky area is shown in bottom left corner of the picture with respect to the full Moon.

galaxies, clusters of galaxies and super-clusters. Due to its complexity, structure formation is theoretically studied using numerical simulations.

In section 1.1, we will briefly describe the cosmological model which is the basis of large-scale structure studies. Section 1.2 will be an overview of the process of structure formation. The problem of substructure dynamics and the need for semi-analytic models of mass loss will be introduced in section 1.3.

1.1 Cosmological Model

Major observations of the 20th century, namely the recession of galaxies and the Cosmic Microwave Background (CMB), point to the fact that the universe is expanding and began by a Big Bang. (Although the exact nature of the initial singularity popularly known as the Big Bang is poorly understood due to the lack of coherent theories of quantum cosmology.) In this context, a theoretical model of the universe is mainly based on Einstein's general theory of relativity. The Einstein field equations in general relativity relate the content of the universe to its geometry. If we assume that the universe is isotropic and homogeneous in scales larger than 100Mpc (a parsec is 3.0857×10^{16} meters or 3.26156 light years), we can derive equations governing the state of the universe (namely the Friedmann equation) from Einstein equations. The assumption of isotropy and homogeneity has proven to be correct from observations of the CMB and large-scale structures in the universe. The Friedmann equation can be written concisely as:

$$\Omega - 1 = \frac{k}{H^2 a^2} \tag{1.1}$$

where $a(t)$ is the so-called *scale factor*, H is the Hubble parameter defined as $H(t) = \frac{\dot{a}(t)}{a(t)}$ and the constant k, describing the spatial curvature, can take the values $k = -1,\ 0,\ +1$. The simplest case, $k = 0$, corresponds to ordinary (flat) Euclidean space. If Ω_i of a substance i in the universe with density ρ_i is defined as $\frac{\rho_i}{\rho_c}$, where $\rho_c \equiv \frac{3H^2}{8\pi G}$ is the density of a flat universe, then Ω is:

$$\Omega = \sum_i \Omega_i \equiv \sum_i \frac{\rho_i}{\rho_c} \tag{1.2}$$

Looking at equation 1.1, we see that a cosmological model of the universe is one that specifies Ω and then the Friedmann equation describes the state of the universe (Ryden, 2003).

Modern observations have given us hints about the content of the universe, in other words Ω's individual constituents. We should note that the various Ω_i evolve differently with time depending on their equation of state. Our current understanding of these main constituents and their contribution to Ω is listed in Table 1.1.

Component	**Contribution to Ω**
CMB radiation	$\Omega_r = 4.7 \times 10^{-5}$
baryons	$\Omega_b = 0.037 \pm 0.009$
(of which stars)	$\Omega_s = (0.0023 - 0.0041) \pm 0.0004$
dark matter	$\Omega_{\rm dm} \simeq 0.3$
dark energy	$\Omega_\Lambda \simeq 0.7$

Table 1.1: The Content of the Universe, from Frenk (2002)

One of the constituents is the CMB radiation. It consists of freely traveling photons coming to us from the time of "recombination" in the early universe, 300000 years after the Big Bang. This radiation field fills the universe.

All matter that we may encounter or experience in everyday life, including our bodies, is composed of atoms and is called *baryonic matter*. Primordial nucleosynthesis and measurements of the Deuterium to Hydrogen abundance ratio D/H in our galaxy and towards quasars result in a precise measurement of the baryon density of the universe (Tytler et al., 2000). Stars make up a small fraction of this density. As we see in Table 1.1, baryons, which interact electromagnetically and thus can be seen, have a small contribution to the content of the universe. According to the standard model of cosmology, most of the universe is invisible!

Most of the invisible matter content of the universe is called "dark matter". We use the term dark matter for a kind of matter whose existence is solely inferred from its gravitational effects.

There are two kinds of observational evidence for the existence of dark matter. The first and most important one is dark matter's dynamical signature. An example of this which is often mentioned as the main evidence for the existence of dark matter is the *rotation curve* of galaxies. A rotation curve is a plot of the orbital velocity of stars or gas in the galaxy versus their distance to the center of the galaxy. Figure 1.2 is the rotation curve of NGC 6503, a spiral galaxy in the Draco constellation. The dotted, dashed and dash-dotted lines are the contributions of gas, stellar disk and dark matter halo, respectively. We see that

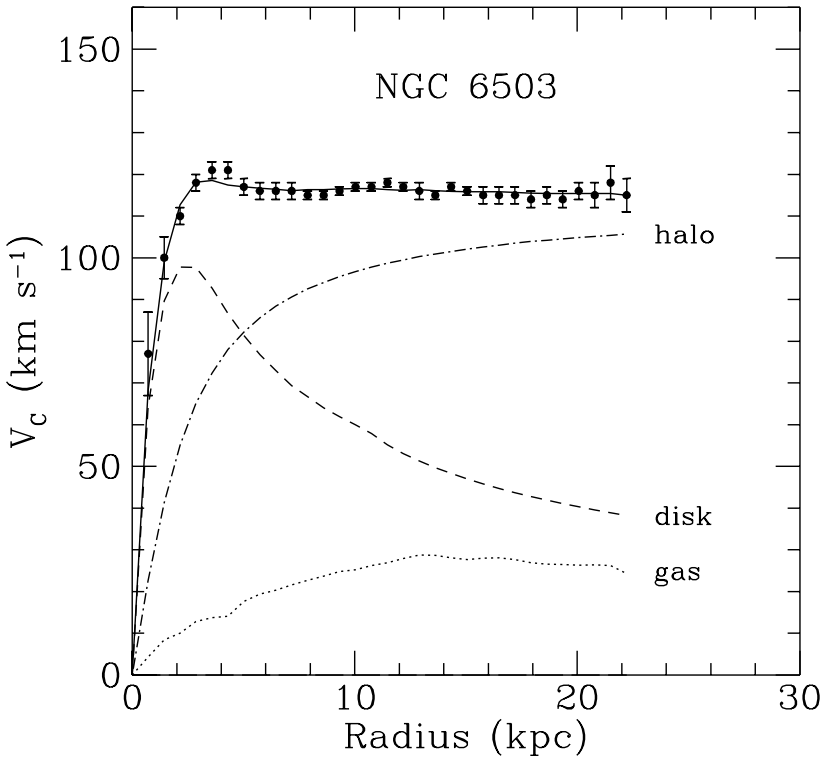

Figure 1.2: Rotation curve of NGC 6503, from Begeman et al. (1991)

the rotation curve flattens as distance increases from the center.

We know that the tangential velocity of an object on a circular orbit induced by a spherical potential ϕ is given by:

$$v_c = \sqrt{R \, \frac{d\phi}{dR}} \tag{1.3}$$

Where R is the distance to the the center of the potential. If the potential of the gravitational force of a spherical mass distribution can be written as $\phi = -\frac{GM(R)}{R}$, then the velocity becomes:

$$v_c = \sqrt{\frac{GM(R)}{R}} \tag{1.4}$$

Where $M(R) = 4\pi \int_0^R \rho(r) r^2 dr$. Therefore if the only matter content of the galaxy were the luminous stars and gas then we would have an increase in velocity up to the

point where mass is increasing faster than distance, and then as we go to longer distances where the mass drops off, the velocity would decrease as $R^{-1/2}$. This would give a rotation curve looking like the dashed curve in Figure 1.2 (disk contribution). The fact that the actual rotation curve is not decreasing at large distances means we must have additional matter in the galaxy. In the simple spherically symmetric case considered here, in order to explain the flatness of the rotation curve we need $M(R) \propto R$ at large R in equation 1.4. In other words, we need $\rho \propto 1/R^2$. This implies the existence of a dark matter halo around the galaxy. Here we considered a spherically symmetric case. However real galaxies are not spherical and halo densities don't decrease as R^{-2}. Observational data coupled with simulations give a more sophisticated distance dependance of the density profile and mass distribution of dark matter halos. These results will be described in section 1.2.2.

A second line of evidence for the existence of dark matter is more direct. The theory of general relativity predicts that light trajectories are bent due to the effect of gravity. This gives rise to a phenomenon called *gravitational lensing*. The image we get from a distant astrophysical object is distorted due to the gravitational field of the intervening matter. If we study statistically these distortions we can infer the mass distribution between us and that object. These image distortions are similar to lens image distortions in optics, thus the name gravitational lensing. As gravitational lensing is solely a "gravitational" phenomenon it can be a probe of the dark matter distribution in the universe. Mellier & van Waerbeke (2001) concisely review the lensing analysis.

If most of the matter content of the universe is dark matter, then the potential dark matter particle should have properties suitable for explaining the formation of structures in the universe from primordial density fluctuations. If dark matter halos consisted of particles with high velocity dispersions in the early universe, this would damp small fluctuations of galactic size and we would end up with a universe without structures of the galactic scale. Therefore dark matter halos should have low velocity dispersions or low *temperatures* in the early universe. In other words dark matter should be "cold" (Blumenthal et al., 1984).

Finally, the last constituent of the universe and the most mysterious one is dark energy. Data from type I supernovae point to the fact that the expansion of the universe is accelerating (Perlmutter et al., 1999). One way of explaining this acceleration is the

cosmological constant Λ first introduced by Einstein. Such a cosmological model with cold dark matter and dark energy as its main constituents is called the ΛCDM model (CDM for cold dark matter) or simply the standard model of cosmology. Given this model, the universe is 13.75 ± 0.11 Gyr old.

1.2 Structure Formation

One of the most interesting questions in cosmology is how structures in the universe formed. By structures we mean objects such as dark matter halos with high matter concentrations compared to their surrounding regions. If we look at the afterglow of the Big Bang, the Cosmic Microwave Background, we can see tiny fluctuations in temperature, that are measures of primordial density fluctuations of matter in the early universe. These primordial fluctuations are the seeds of all structure in the universe. The origin of these tiny fluctuations can be explained quantum mechanically in the context of cosmic inflation. The statistical properties of the primordial fluctuations can be inferred from observations of anisotropies in the Cosmic Microwave Background (Spergel et al., 2003) and from measurements of the distribution of matter, e.g., galaxy redshift surveys. If we break the density fluctuations into an infinite number of sine waves with different components δ_k, and comoving wavenumbers k, then the power spectrum is defined as the mean square amplitude of the components $P(k) = \langle|\delta_k|^2\rangle$. Most inflationary scenarios result in a power-law form of the power spectrum $P(k) \propto k^n$. In a universe with this initial power spectrum, fluctuations in the cold dark matter are largest in amplitude for the smallest mass scales. This implies that in such a universe, the first objects to form are the smallest. This is called the *hierarchical* scenario of structure formation. If the dark matter particle is the *neutralino* (a hypothetical particle with mass $m \simeq 100$ GeV predicted by supersymmetry) then $P(k) \propto k^3$ with an exponential cut-off at 0.6 comoving parsecs which corresponds to a mass scale of 10^{-6} solar masses (Green et al., 2004). This is roughly the mass scale of the first and smallest dark matter halos that form in the early universe. In order to understand how these first structures form, we can imagine the primordial universe to be divided in overdense and under dense regions according to the CMB maps. The overdense regions

have a tendency to collapse under their own gravity, but at the same time the universe is expanding. Therefore self-gravity and expansion work against each other. For regions with overall negative energy (the energy is an integral of motion and a function of initial conditions), at first expansion wins and the overdense region expands while its self-gravity slowly increases. At some critical time, the process is reversed to the profit of the now equally powerful self-gravity. At this moment (called *turnaround*) the structure begins to collapse, and eventually forms a bound object. The detailed mathematics of structure formation and non-linear evolution can be found in Padmanabhan (1993).

1.2.1 Formation of Dark Matter Halos

The radius at which the overdense region starts to collapse is called the *turnaround radius*, r_m. It is a function of the initial conditions (initial background density Ω_i and density fluctuation δ_i). Having initial conditions we can not only find r_m but we can also derive the time evolution of the overdense region. If the problem was completely symmetrical (for instance if the overdensity was spherical and the velocities of all the particles were oriented towards the center of the sphere) the overdense region would collapse through a central point and expand outwards afterwards. But the symmetrical assumption doesn't hold for real systems. Because of the random motions of particles, and also due to the change of the potential in a timescale of $t_{dyn} \approx (G\rho)^{-1/2}$, much shorter than the two-body relaxation time t_R, the collisionless dark matter will be "violently" relaxed to a configuration with radius $r_{vir} = r_m/2$, and a special density profile and velocity dispersion (Padmanabhan, 1993). This process is called *virialization* and gives rise to an approximately stable, near-equilibrium dark matter halo. The halo is supported against its own self-gravity by the random motions of its particles.

As mentioned above, each particle in a virialized halo is on an orbit with a particular energy. Due to the extremely large number of particles and the chaotic nature of the problem, modeling theoretically such a halo and its merging with another halo is extremely difficult. That is why we study structure formation using N-body numerical simulations (although there are a number of successful theoretical models such as the Press & Schechter (1974) formalism for predicting the abundance of halos of a given mass within a given

volume of the universe). One example of such simulations is the Millennium simulation (Springel et al., 2005). If the simulation is solely composed of dark matter it has to make relatively few assumptions as the physics of gravitationally interacting matter in cosmological scales is simple. However if the simulation also includes baryons then it has to make more assumptions about baryonic processes that are complicated as they are of electromagnetic nature.

One of the successful results of simulations that appears to be correct observationally is the universal density profile of dark matter halos. Many theoretical models, as the ones discussed in this thesis, need to assume this density profile.

1.2.2 Structure of Dark Matter Halos

As mentioned in section 1.1, one of the observational lines of evidence for the existence of dark matter halos is the rotation curve of galaxies. In our simple approach to the problem in section 1.1, we explained the flattening of the rotation curve by assigning a density profile $\rho(r) \propto 1/r^2$ to the dark matter halo. Such a profile known as the isothermal profile was widely used before the 90s to model virialized dark matter halos. This profile gives rise to constant velocity dispersions therefore we can assign a constant temperature to it, thus the name isothermal. It has been plotted versus distance in log scale as the dashed line in figure 1.3.

The numerical simulations of Navarro, Frenk and White (and others) suggest that the density profile of halos are not well approximated by isothermal profiles but rather have gently changing logarithmic slopes (Navarro et al., 1996). The NFW density profile has the form:

$$\rho_{NFW}(r) = \frac{\rho_s}{r/r_s(1 + r/r_s)^2} \tag{1.5}$$

Where ρ_s is the scale density and r_s is the scale radius. This profile is plotted as the solid curve in figure 1.3. As we see in the figure, the behavior of the NFW profile is almost isothermal near $r = r_s$.

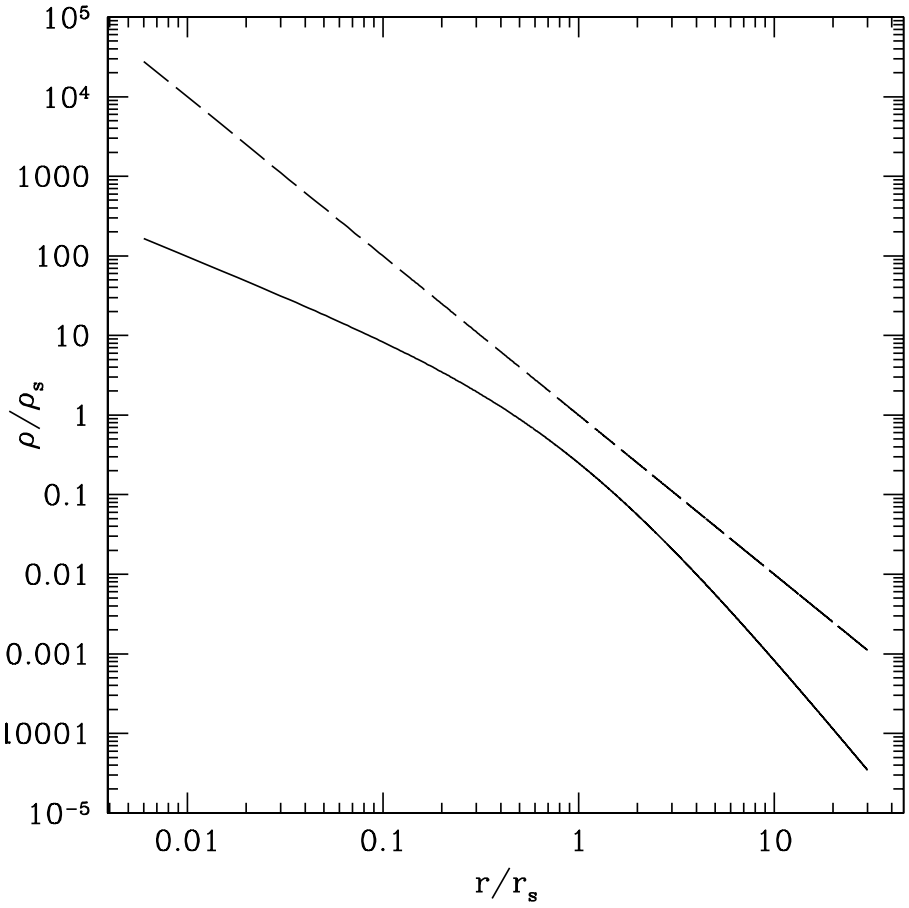

Figure 1.3: The NFW density profile (solid) and the isothermal density profile (dashed) as a function of radius.

Recent studies by Navarro et al. (2004) have shown that dark matter halos are slightly better described by an Einasto density profile. This profile has the form:

$$\rho(r) \propto \exp\big(-A\ r^{\alpha}\big) \tag{1.6}$$

Where the parameter α controls the degree of curvature of the profile. The NFW profile is good to within 10 to 20% making it still useful (Benson, 2010). The radius inside which the virial equilibrium holds in a dark matter halo is called the virial radius r_{vir}. The concentration of the halo is defined as $c_{NFW} = r_{vir}/r_s$.

1.3 Substructure Dynamics

For a long time it was believed that in the hierarchical picture of structure formation, as each halo is formed from the merging of smaller halos any sign of the progenitors is erased due to their complete disruption. Early simulations seemed to confirm this assumption. As simulations grew in resolution in the 90s, they uncovered a wealth of subhalos that had remained bound after merging had happened and were on orbits around their host halos (Klypin et al., 1999; Moore et al., 1999).

Subhalos more massive than 10^9 to 10^{10} $M_\odot$ (solar masses) host galaxies that evolve in bigger systems such as clusters of galaxies. We need to understand the dynamics of galaxies within clusters in order to know more about galaxy formation and evolution. These galaxy dynamics are closely related to the collisionless dynamics of sub-halos within bigger halos of dark matter. Substructure evolution, as other fields of structure formation can be studied using cosmological simulations. Unfortunately, this approach has two major inconveniences: first an foremost the lack of resolution (in mass, force field and time) of cosmological simulations at sub-halo scales limits their use. The second reason is the computational costs and resources they require. An analytic approach to the problem is useful because it independently provides insight in issues related to galaxy formation and evolution in cluster environments.

If resolution limits affect the accuracy of cosmological simulations in the study of galaxies, they make it impossible to study dark matter halos in smaller scales such as the scale of the solar system. In order to study galaxy formation, a spatial resolution better than 1 kpc and a mass resolution better than 10^6 $M_\odot$ in volumes at least 100 Mpc across containing more than 10^{17} $M_\odot$ is required (Bertschinger, 2001). This means that galaxy formation can be effectively studied using cosmological simulations with $\simeq 10^{11}$ particles. With computational advances we are slowly reaching this resolution. Figure 1.4 shows the particle number in cosmological simulations as a function of publication date. As seen in the figure the growth in simulation size has been exponential over the last three decades. However if we want to study dark matter in small scales such as 1 AU (the Astronomical Unit is roughly equal to the length of the semi-major axis of the Earth's elliptical orbit around the Sun $\simeq 10^{-6}$ parsecs) in similar cosmological volumes, we will roughly need 10^{20} particles

with masses of $10^{-3}\ M_{\odot}$ (having in mind that the mass scale of the smallest dark matter halos is of order $10^{-6}\ M_{\odot}$ thus lower particle masses are required). Looking at figure 1.4 we see that this would not be computationally possible in the next 50 years. Many dark matter detection experiments are based on the annihilation of dark matter particles (neutralinos) resulting in Gamma rays. This annihilation rate is proportional to the square of the density of dark matter. Therefore, if we hope to eventually detect the dark matter particle it will be extremely helpful to know how dark matter is distributed and how dense dark matter clumps are locally. To overcome the resolution limits imposed on cosmic simulations, Diemand et al. (2005) carried out a large cosmological simulation and re-simulated at higher resolution a small region of it. The simulation started at redshift $z = 350$ and followed the evolution of the higher resolution region until redshift $z = 26$ when it started to merge into the lower resolution surroundings. The authors found that the first halos to form are triaxial objects of mass $10^{-6}\ M_{\odot}$. These objects did not have substructures in them as they were the first to form in the hierarchy. The density of these sub-halos was well fitted by a power law form $\rho(r) \propto r^{-\gamma}$ where γ was in the range from 1.5 to 2. The authors also found the mass function of the halos and estimated their number density at the solar radius as $n(R_{\odot}) \simeq 500\ pc^{-3}$.

As only a small region of such a simulation has high resolution, predicting the interaction of these subhalos with galaxies and even stars (as the first subhalos to form have little mass and are affected by the motion of stars) can not be done numerically and requires analytic models describing subhalo mergers and predicting whether substructures get disrupted by galactic gravitational forces or stay bound. Diemand et al. (2005) analytically predicted that the small halos of dark matter could stay bound to about 3 kpc from the center of the galaxy. As encounters with stars could result in the disruption of halos, Green & Goodwin (2007) studied, analytically and numerically, the energy input into dark matter mini-haloes by interactions with stars. They found that for mini-haloes with mass $M < 10^{-7}\ M_{\odot}$ on typical orbits which pass through the galactic disc, the estimated disruption time-scales are independent of mini-halo mass, and are of the order of the age of the Milky Way. The authors also found that for more massive mini-haloes, the estimated disruption time-scales increase rapidly with increasing mass.

Because of the complexity of the problem an analytic model of substructure evolution will be approximative. The validity of the approximations it makes can be tested with numerical simulations of substructure evolution. Then such a semi-analytic model will be useful where cosmological simulations are of no help. These semi-analytic models should describe important physical phenomena going on in minor mergers, and predict how subhalos lose mass on their orbit in the host halo.

Semi-analytic models of mass loss usually take into account two major processes: Dynamical friction and tidal interactions: (a) *Dynamical friction* is due to the subhalo traveling through a sea of dark matter particles. As the subhalo gravitationally drags the particles and forms a region of higher density behind it, it suffers a steady deceleration due to the gravity of that dense region. The effect of this friction on the motion of the subhalo around the host is the shrinking of its orbit. (b) *Tidal interactions* are due to the inequality of the gravitational forces from the host on different parts of the subhalo. These tidal forces strip away the outer regions of the satellite and might even result in its disruption. In addition to this unbinding effect on the outer regions of the satellite, tidal forces can also heat the inner regions of the satellite and result in its expansion that would in turn result in more mass loss. Tidal stripping reduces the mass of the satellite and as a result reduces the effect of dynamical friction. Therefore tidal interactions and dynamical friction work against each other to some degree.

Taylor & Babul (2001) have developed a simple analytic scheme that accounts for these processes. The parameters of the model were calibrated to fit the numerical results of Velazquez & White (1999). Athough the model matches simulations very well, there are some discrepancies found. The high sensitivity of the satellite evolution to its density profile was suggested by the authors as a possible explanation for these discrepancies.

Does heating for instance affect the density profile of the subhalo? Hayashi et al. (2003) have found that the density profile of satellites changes as a function of their bound mass throughout their evolution and Kazantzidis et al. (2004b) have found that the density profiles of substructure halos can be well fitted with a power-law central slope that is unmodified by tidal forces even after the tidal stripping of over 99% of the initial mass and an exponential cutoff in the outer parts. Another question about heating is how it

transfers energy to the satellite. Green & Goodwin (2007) have found that the fractional energy input in simulations agrees well with the impulse approximation. The Taylor & Babul model also uses the impulse approximation to calculate heating.

As dynamical friction decreases when the ratio M_{host}/M_{sat} increases, for a situation in which the mass of the satellite is much smaller than the mass of the halo the effect of dynamical friction is small. In addition dynamical friction is relatively easy to model analytically while modeling mass loss is much harder (Taylor & Babul, 2001). Therefore it is useful to isolate heating from other effects such as dynamical friction in order to study it. To do so in this thesis we consider a satellite orbiting around a host. The host will be a static non-discretized NFW potential. As a result we will not have dynamical friction. The satellite will lose mass due to tidal stripping and heating only. We will use the simulations described in chapter 2 to compare our model with. The tidal approximation, impulse approximation and a model incorporating both will be described in chapter 3. In chapter 4 we will adjust the parameters of the model based on energy criteria to fit numerical results. We will also look at the change of the density profile and its effects on mass loss. Finally in chapter 5 we will look at the effect of resolution on the evolution of the subhalo.

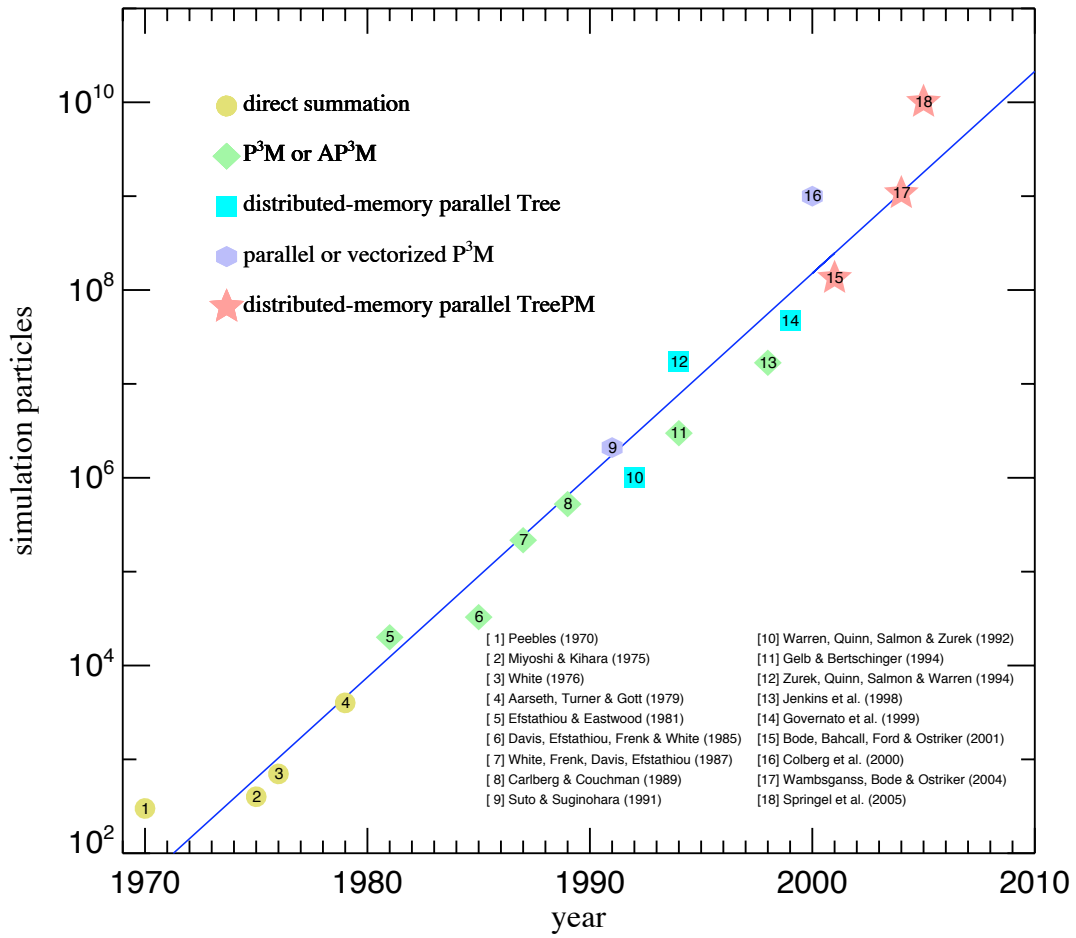

Figure 1.4: Particle number in high-resolution N-body simulations of cosmic structure as a function of publication date, from Springel et al. (2005)

Chapter 2

The Simulations

We need to simulate a satellite (or substructure) orbiting in a spherically symmetric dark matter halo. Such a problem has two components: (a) *The Halo*: As we are neglecting the effect of dynamical friction we do not need to discretize the halo. Therefore the halo will be simply represented by a static NFW density profile. The parameters of such a profile will be described in section 2.1.1. (b) *The Satellite* will be discretized with N particles. In the highest resolution $N = 10^5$. The customary way to adjust the initial conditions of the satellite will be briefly reviewed in 2.1.2. The satellite will first evolve in isolation to reach equilibrium and then will evolve in the gravitational field of the background halo. In section 2.2 the code that simulates this evolution as well as the orbit of the satellite in the halo will be discussed. Finally in section 2.3 we will look at how the satellite loses mass according to the numerical results. The simulations analyzed here were originally carried out by Andrew Benson, Eric Hayashi and Carlo Nipoti.

2.1 Initial Conditions

The simulations were run to produce two sets of data for this research. The two sets correspond to two orbits with different parameters including different initial conditions for the satellite and the halo. As one of the orbits is more eccentric than the other we will call one OrbitC (more circular) and the other OrbitE (more eccentric).

2.1.1 Background Halo

The halo is a static NFW profile (Navarro et al., 1996). This density profile is given by:

$$\rho_{NFW} = \frac{\rho_s}{r/r_s(1+r/r_s)^2} \tag{2.1}$$

Where r_s is the scale radius. As the scale radius gives us the relative scales of the halo and the satellite, we will choose $r_{s,\ satellite} = 1$ for the two orbits. For OrbitC, $r_{s,\ halo} = 16$ and for OrbitE, $r_{s,\ halo} = 4$. We can find the mass enclosed in radius R by:

$$M(< R) = 4\pi \int_0^R \rho_{NFW}(r) r^2 dr = 4\pi \int_0^R \frac{\rho_s}{r/r_s(1+r/r_s)^2} r^2 dr \tag{2.2}$$

$$M(< R) = 4\pi\rho_s r_s^3 \Big[\ln(\frac{r_s+R}{r_s}) - \frac{R}{r_s+R} \Big] \tag{2.3}$$

This expression goes to infinity when $R \to \infty$. We conventionally define the mass of the halo as its virialized mass, that is the mass within the virial radius r_{vir}. Therefore the profile can be truncated at this radius. However a sharp truncation does not correspond to a physical system. Springel & White (1999) and Kazantzidis et al. (2004a) have used an exponential cutoff for $r > r_{vir}$. This cutoff starts at the virial radius and turns off the density profile on a scale r_{decay}.

We defined the concentration of a dark matter halo as $c = r_{vir}/r_s$ in the introduction. The concentration of the background halo is $c_{halo} = 8$ for OrbitC and $c_{halo} = 4$ for OrbitE. The mass of the halo enclosed in the virial radius is given by:

$$M(< r_{vir}) = 4\pi\rho_s r_s^3 \left[\ln(\frac{r_s+r_{vir}}{r_s}) - \frac{r_{vir}}{r_s+r_{vir}} \right] \tag{2.4}$$

From the definition of concentration we can rewrite this as:

$$M(< r_{vir}) = 4\pi\rho_s r_s^3 \left[\ln(1+c) - \frac{c}{1+c} \right] \tag{2.5}$$

Parameter	**OrbitC**	**OrbitE**
$r_{s_{halo}}$	16	4
$r_{s_{satellite}}$	1	1
c_{halo}	8	4
$c_{satellite}$	16	4
$M_{vir_{halo}}$	512	64
$M_{vir_{satellite}}$	1	1

Table 2.1: The NFW Profile Parameters

The virial mass of the halo $M(< r_{vir})$ or simply M_{vir} is one of the parameters of the problem. We choose our units so that the virial mass of the satellite is one and the virial mass of the halo is $M_{vir} = 512$ for OrbitC and $M_{vir} = 64$ for OrbitE. If we choose the scale radius r_s, the concentration c and the virial mass M_{vir} as the main parameters of the halo profile, the scale density will be a function of these parameters (from equ. 2.5):

$$\rho_s = \frac{M_{vir}}{4\pi r_s^3} \frac{1}{\ln(1+c) - c/(1+c)} \tag{2.6}$$

In table 2.1, the NFW profile parameters of the two numerical orbits are summarized. Having defined our halo with its density parameters, we can now find its gravitational potential. After all the only effect of the halo in our problem is the gravitational field it induces on the satellite. As the halo is spherically symmetric its gravitational potential $\phi(r)$ at radius r will be the sum of two terms (Binney & Tremaine, 1994):

$$\phi(r) = -4\pi G \left[\frac{1}{r}\int_0^r \rho(r')r'^2 dr' + \int_r^\infty \rho(r')r' dr'\right] \tag{2.7}$$

The first term is equivalent to the potential of the mass enclosed inside radius r, $\phi_1(r) = -\frac{GM(<r)}{r}$. The second term is the sum of the potentials of individual spherical shells from radius r to ∞. If we take the above integrals for the NFW density profile (equ. 2.1), we find the following expression:

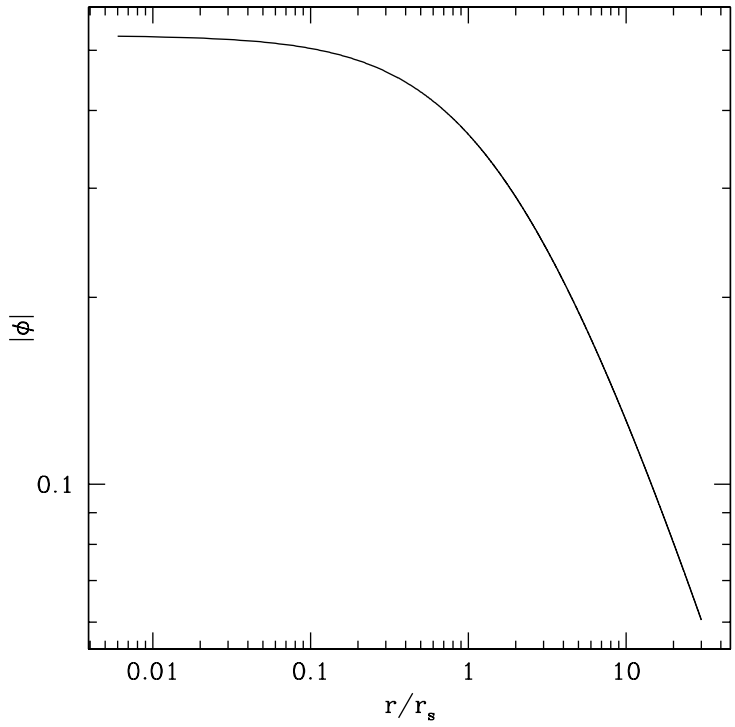

Figure 2.1: The absolute value of the NFW potential of the background halo.

$$\phi(r) = -4\pi G\rho_s r_s^3 \ \ \frac{\ln(1+r/r_s)}{r} \tag{2.8}$$

If we use equ. 2.6 to substitute for ρ_s we find:

$$\phi(r) = -\frac{GM_{vir}}{r} \ \ \frac{\ln(1+r/r_s)}{\ln(1+c)-c/(1+c)} \tag{2.9}$$

Figure 2.1 shows $-\phi(r)$ versus r in log scale for the halo parameters of OrbitC (table 2.1). We set $G = 1$ throughout this thesis. As $G = 4.4987 \times 10^{-3} pc^3 M_\odot^{-1} Myr^{-2}$, setting G equal to 1 will fix the time unit of the problem given the distance and mass units. For instance for a length unit of 1 pc and a mass unit of 1 solar mass, the time unit is 14.91 Myr ($\approx t_H/1000$). For a length unit of 1 kpc and a mass unit of $10^9 M_\odot$, the time unit is the same. For a length unit of 10 kpc and a mass unit of $10^9 M_\odot$, the time unit is 471.5 Myr ($\approx t_H/30$), where $t_H \equiv 1/H_0 \approx 13.8$ Gyr.

It is worth mentioning that as the background halo is static and doesn't evolve numerically all of the above quantities could be found analytically. The situation is more complicated for the satellite.

2.1.2 Satellite

We would like the satellite to have the same initial density profile as the halo, because the satellite is a sub-halo and the NFW profile is universal. But the satellite consists of N particles. Therefore we should find a distribution of particles that would result in an NFW profile. A collisionless system of particles is fully described by its distribution function $f(x, v, t)$, giving the number of particles centered at position x in the volume d^3x with velocities centered around v in the small range d^3v. Such a function satisfies the collisionless Boltzmann equation (Binney & Tremaine, 1994):

$$\frac{\partial f}{\partial t} + v \cdot \nabla f - \nabla \phi \cdot \frac{\partial f}{\partial v} = 0 \tag{2.10}$$

If we have this distribution function the spatial density $\rho(r)$ can be easily found:

$$\rho(r) = \int f(r, v)\ d^3v \tag{2.11}$$

The inversion of the above integral gives the distribution function as a function of the density profile given that the velocity distribution of the satellite should support it against its self-gravity and be in equilibrium. As $\rho(r)$ is a function of position only and $f(r, v)$ is a function of both the position and velocity, this inversion is difficult and involves making assumptions about the velocities of particles. It has been first studied by Eddington (1916). Different methods have been used to find suitable equilibrium distribution functions for the NFW profile.

To avoid this difficult inversion, the velocity distribution of the satellite is taken to be Maxwellian initially, in other words:

$$f(r, v) = 4\pi \big(\frac{1}{2\pi\sigma^2}\big)^{3/2}\ v^2\ \exp(-v^2/2\overline{v_r^2}) \tag{2.12}$$

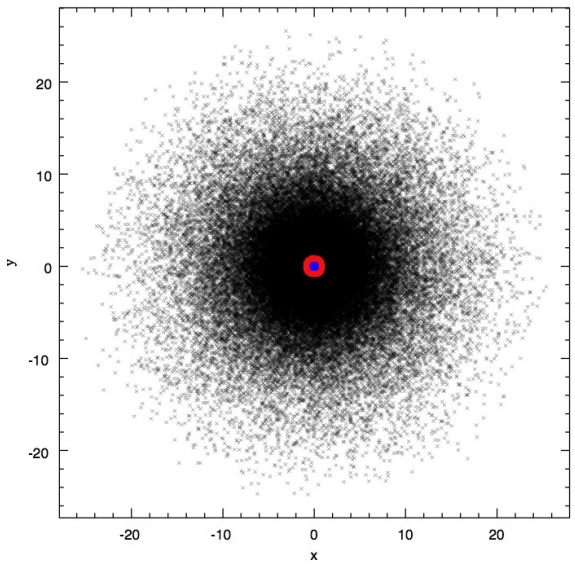

Figure 2.2: Satellite at time zero: The red contour shows the scale radius $r = r_s = 1$ and the blue region in the middle corresponds to $r < 0.3$ where the density falls below the NFW profile as seen in 2.3

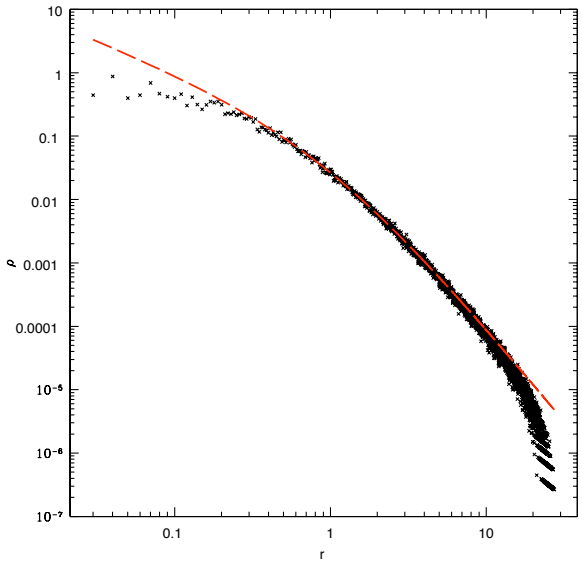

Figure 2.3: Satellite's initial density in log scale: The black dots are the densities of thin shells of radius r and thickness $dr = 0.004$. The red dashed curve is the theoretical NFW density profile.

Where:

$$\overline{v_r^2} = \frac{1}{\rho(r)} \int_r^\infty \rho(r') \frac{GM(r')}{r'^2} \, dr' \tag{2.13}$$

This in turn is given by the second moment of the collisionless Boltzmann equation assuming the profile is initially spherical and isotropic (Hernquist, 1993). The satellite is then allowed to relax in isolation before the main potential is turned on. Figure 2.2 shows the xy projection of the satellite's final mass distribution with the concentration parameter $c = 16$. Thus the virial radius is 16 as the scale radius of the satellite is set to 1. We see that the satellite has been exponentially truncated after radius 16 instead of a sharp truncation. Figure 2.3 shows the density profile of the satellite. Each of the black dots is the average density of a thin shell of thickness $dr = 0.004$ centered at radius r. The red dashed curve is the analytical NFW density profile given by equ. 2.1 with density parameters $c = 16$, $r_s = 1$ and $M_{vir} = 1$.

We see that the density of the satellite falls below the NFW density in radii larger than $r_{vir} = 16$. This is due to the exponential cutoff imposed on the satellite. The density is almost exactly NFW at smaller radii until around $r = 0.3$ where it falls below the NFW density again. The $r < 0.3$ region corresponds to the blue region in the middle of the satellite in figure 2.2. This discrepancy is probably due to the softening length of the simulation being larger than the central radii. In the highest resolution simulation ($N = 10^5$), the softening length is $\epsilon \simeq 0.126$ in the units described in section 2.1.1 where $r_s = 1$. The discrepancy may also arise after the isolated evolution of the satellite because the initial distribution function has not exactly been in equilibrium. Kazantzidis et al. (2004a) have shown that this behavior is seen in locally Maxwellian distributions and have introduced methods to produce equilibrium distribution functions.

Figure 2.4 illustrates the radial velocity dispersion of the satellite. Each dot is the velocity dispersion $\sigma_r = \overline{(v_r - \overline{v_r})^2}$ calculated in a thin shell of thickness $dr = 0.004$ centered at radius r. We see that the radial velocity dispersion has its maximum at $r = r_s = 1$ where the behavior of the profile is isothermal as seen in figure 1.3.

2.2 Evolution of the Satellite

Given this initial distribution of particles of the satellite that results in a near-equilibrium NFW profile, the center of mass of the satellite will be given an initial velocity and the satellite will start orbiting in the gravitational potential of the background halo. Each particle of the satellite will feel the gravitational field of the other particles in addition to the gravity of the background halo. The code that has been used to simulate the motion of particles and the evolution of the satellite is called GADGET (GAlaxies with Dark matter and Gas intEracT). It has been developed by Springel et al. (2001). As its name indicates the code was originally designed to simulate both the baryonic component and the dark matter component of the galaxy. Here only the gravitational part of the code has been used as we do not have gas in our problem. In GADGET, as in most other N-body simulations of collisionless dark matter, a softening length is introduced in the gravitational potential in small separations. This is done to avoid large-angle scatterings in two-particle collisions, as

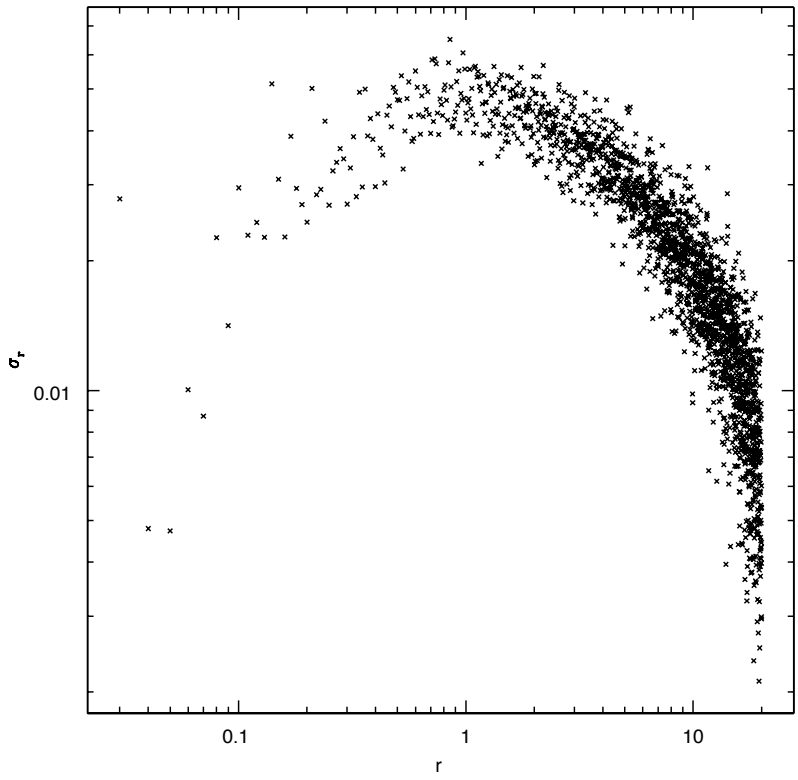

Figure 2.4: Satellite's initial velocity dispersion. Each dot is the velocity dispersion calculated in a shell of thickness $dr = 0.004$ at radius r.

the particles used in the simulations are 10^{70} times more massive than the Gev candidates for the dark matter particle. This softening length imposes a *spatial resolution limit*. As mentioned in the previous section, the softening length is $\epsilon \simeq 0.126$ in the units where $r_s = 1$ in the highest resolution simulation ($N = 10^5$). To decrease the effect of two-body relaxation, we need to increase the number of particles in the simulation. The effect of two-body relaxation on the evolution of the satellite and the problem of resolution limits will be inspected in more detail in chapter 5.

GADGET uses a tree method to calculate the gravitational forces between the particles. In this method the particles are arranged in different groups. Instead of calculating the force on each particle from all the other particles, GADGET finds the low-multipole

approximation of the force on the particle from each distant group. In this way the computational cost is reduced to order $N\log(N)$, where N is the number of particles. This imposes a *force resolution limit*. The force becomes more accurate in higher moments of the multipole expansion, but to make the code efficient the multipole expansion is cut at the quadropole.

As a time integrator, GADGET uses a variant of the Leapfrog method, which introduces a *time resolution* (for details see Springel et al. (2001)). In this simulation we follow the evolution of the satellite in 50 time steps. Theoretically, the orbit of an object in a spherical gravitational potential is governed by Newton's law of motion:

$$\frac{d^2\overrightarrow{r}}{dt^2} = F(r)\hat{e}_r \tag{2.14}$$

Where $F(r)$ is the force per unit mass. If we use plane polar coordinates (r, ψ) we find:

$$\ddot{r} - r\dot{\psi}^2 = F(r) \tag{2.15}$$

$$2\dot{r}\dot{\psi} + r\ddot{\psi} = 0 \tag{2.16}$$

Integrating the second equation gives one of the integrals of motion, the angular momentum:

$$r^2\dot{\psi} = constant \equiv L \tag{2.17}$$

And integrating the first equation (see Binney & Tremaine (1994)) gives another integral of motion, the energy:

$$E = \frac{1}{2}\dot{r}^2 + \frac{1}{2}(r\dot{\psi})^2 + \phi(r) \tag{2.18}$$

Therefore to constrain the orbit of the satellite we need the initial r, $\dot{r}$ and $\dot{\psi}$. In both OrbitC and OrbitE, we start at apocenter so $\dot{r}_{initial}$ is set to 0. If L_c is defined as the angular momentum of a circular orbit with the same energy, the circularity parameter e is defined as $e = L/L_c$. The orbits are chosen to have specific values of e. In OrbitC the satellite is given a tangential velocity $\dot{\psi} = v_t = 1.34396$ at its apocenter $r = r_a = 171.4336$ and in OrbitE a tangential velocity $\dot{\psi} = v_t = 0.76242$ at the apocenter $r = r_a = 25.183$. These choices result in circularity parameter $e = 0.9$ for OrbitC and $e = 0.6$ for OrbitE. These two orbits are illustrated respectively in figure 2.5 and figure 2.6. As we see OrbitE is

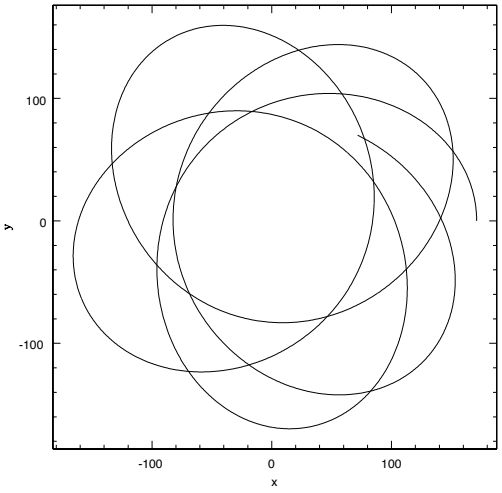

Figure 2.5: OrbitC

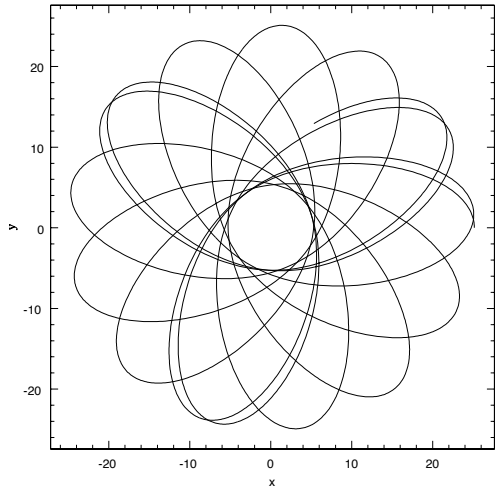

Figure 2.6: OrbitE

more eccentric. Both orbits form a "rosette" which is the typical form of orbits in spherical potentials. The orbits precess backwards, at a precession rate which can be analytically calculated having the energy and angular momentum of the orbit (Binney & Tremaine, 1994). Giving the center of mass of the satellite its initial orbital position and tangential velocity, GADGET simulates its evolution in the next 50 outputs.

Figure 2.7 shows this evolution. The yellow points are the positions of the center of mass of the satellite. The satellite starts in the top left plot at the apocenter of its orbit with the initial conditions described above. Then as it moves on the orbit in subsequent steps it forms tidal arms backward and forward, one of the arms inside the orbit and the other outside. The particles in the arms are the ones that are more under the effect of the background potential than the potential of the satellite and have separated or become "unbound". The dense core of the satellite stays bound (see figure 2.9).

As we see in figure 2.7, the orbit of the satellite does not shrink. If we had discretized the background halo then dynamical friction would have slowed the satellite and made it go to smaller radii. Here as the apocenter distance r_a stays constant the satellite loses mass solely due to its tidal interactions with the background halo. These tidal interactions are responsible for producing the tidal arms of the satellite.

2.3 Mass Loss

To be able to ask how much of the mass of the satellite gets lost as it orbits in the background halo, we should first specify what we mean by bound mass. There is a useful iterative criterion for specifying the particles that are gravitationally captured by the satellite and are thus bound to it. This criterion was first introduced by Tormen et al. (1998). In each step:

(1) Only the particles are chosen that were bound at the previous time step. For instance at $step = 0$ these will be all the particles of the satellite and at $step = 1$ the particles bound in $step = 0$.

(2) The total energy of each particle is calculated by summing the potential energy resulting from the distribution of the satellite's particles and the kinetic energy calculated in a reference frame moving with the average velocity of all particles.

(3) Particles with positive energy are removed.

(4) Energies are calculated again using the new set of particles.

The last two steps are repeated until the number of bound particles (with negative energy) doesn't change. This gives a numerical measure of the bound mass of the satellite. Figure 2.8 shows the fraction of the bound mass of the satellite versus time step. We see this fraction decreases steeply at first and eventually flattens. Mass loss occurs rapidly around the pericenter of each orbit, and slows at apocenter. About 40% of the mass stays bound at the end. Figure 2.9 illustrates the satellite at its zeroth time step. The particles are colored with their unbinding step. As we see the particles in the dense core of the satellite with $r < 4$ (for OrbitC) stay bound to the satellite until the last time step.

This measure for the self-bound mass of the satellite has two shortcomings and therefore should be considered as a good approximation of mass loss rather than an exact criterion. The first one is that it definitely unbinds particles, which means that as soon as a particle's energy goes positive in a certain time step of the simulation it definitely gets unbound. This gives rise to the perfectly monotonic decrease of mass seen in figure 2.8. However in reality it takes time for a particle's velocity to reach the velocity dispersion of the background halo

and thus it might stay around the satellite for a while and thus might be recaptured by the satellite's gravitational field. This suggests that a better mass loss curve would have small fluctuations rather than being perfectly monotonic. As these fluctuations are very small and we worry mainly about the long term evolution of the satellite this can be neglected. A second problem is that the criterion is energy based. In other words it assumes that only particles with negative energies are bound to the satellite. However, energy is not the only integral of motion for a particle's orbit. Other integrals of motion can give rise to bound orbits around the satellite. The theoretical treatment of these integrals of motion is described in detail in Binney & Tremaine (1994). The authors as well as others they refer to have argued that the phase-space density of these kinds of orbits decreases rapidly after the so-called *tidal radius* of the satellite described in the next chapter. Therefore this second shortcoming doesn't introduce much error either.

As a result, we will choose this numerical criterion as a trustable measure of the bound mass of the satellite. In the next chapters we will analytically model mass loss. Figure 2.8 will be our reference mass loss curve, as the main purpose of our semi-analytic model is to predict mass loss as closely as possible to the numerical iterative result.

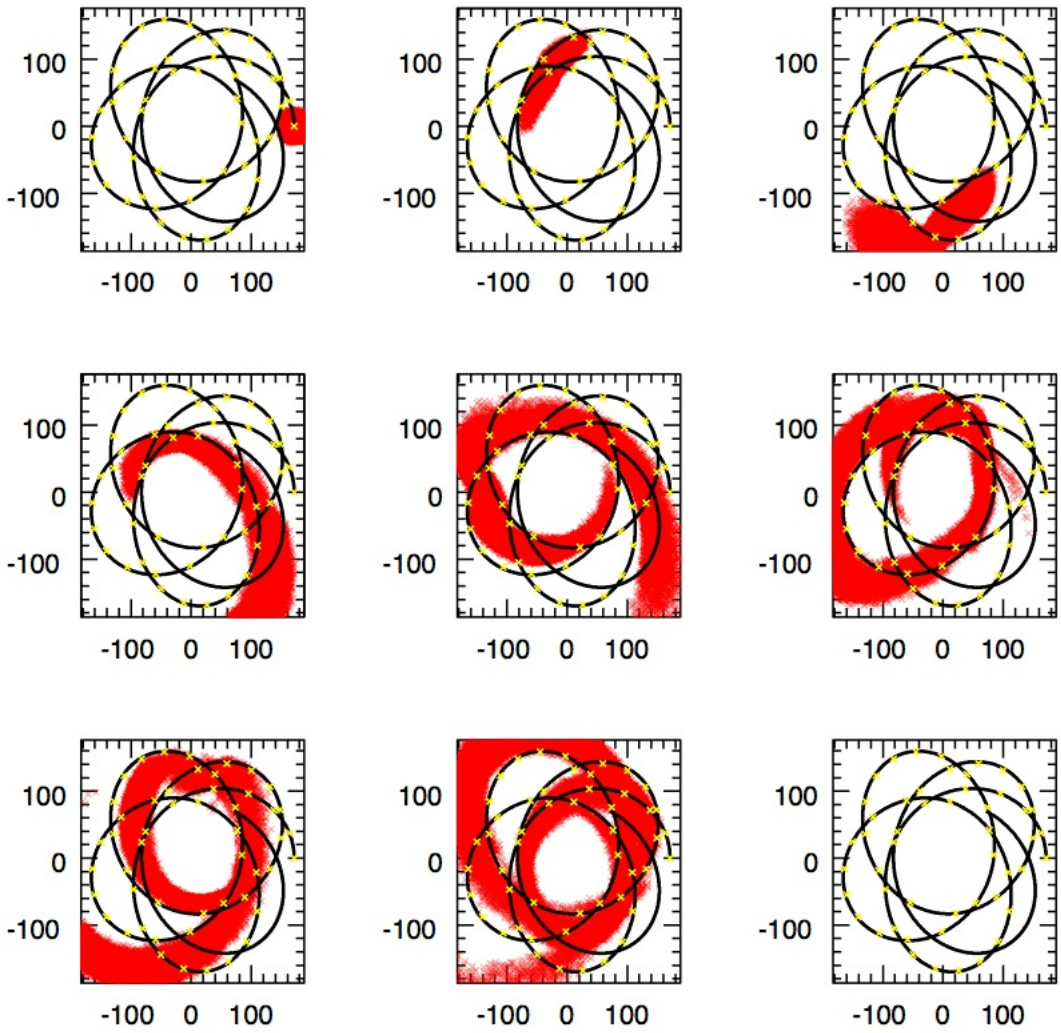

Figure 2.7: Evolution of the satellite in OrbitC: The bottom right plot shows OrbitC with the yellow dots on it representing the center of mass of the satellite in 50 steps of the simulation. From top left to right we see the evolution of the satellite in time steps 0, 5, 10, 15, 20, 25, 30 and 40 of the simulation.

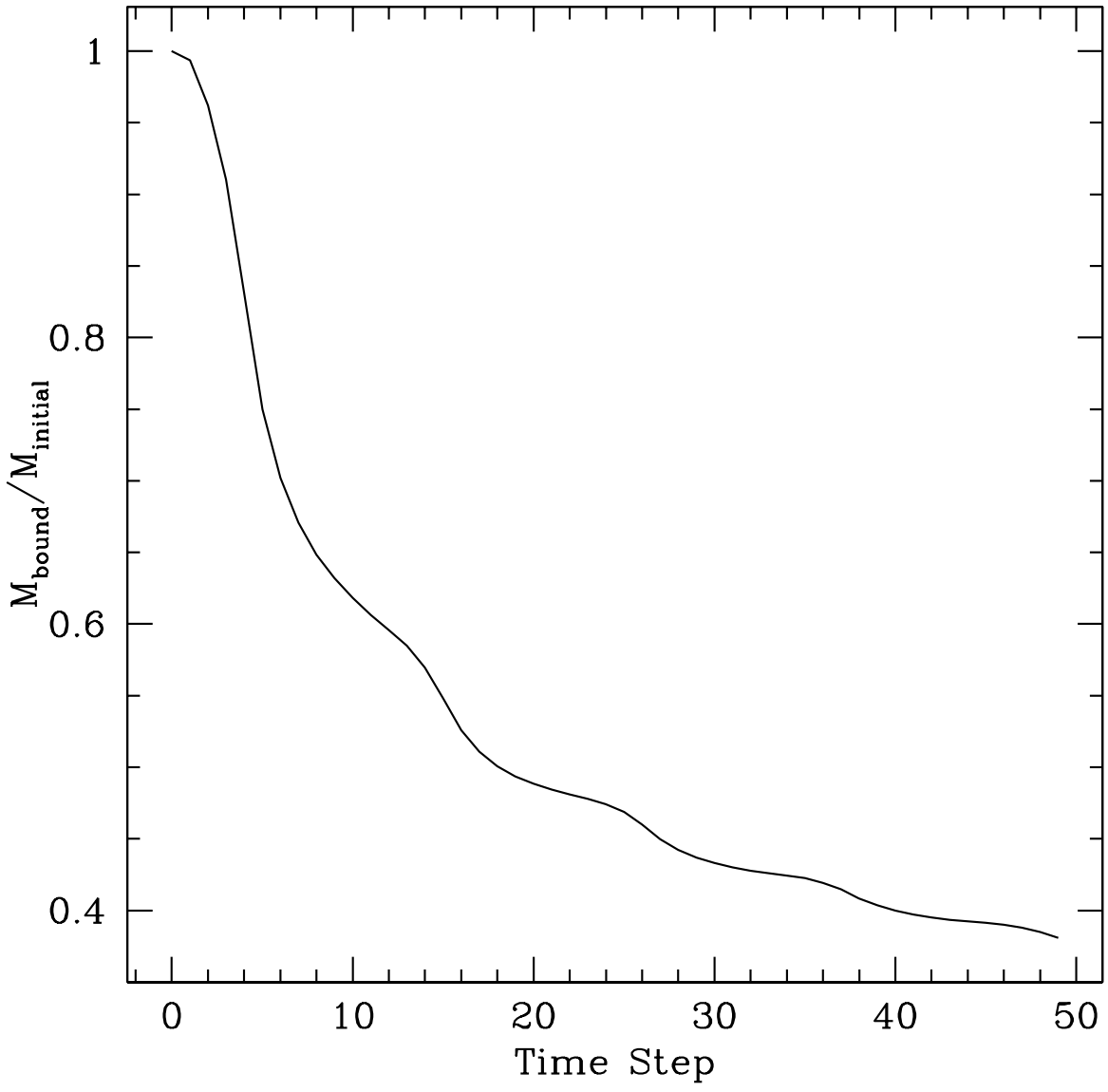

Figure 2.8: Mass Loss: M_{bound} versus $M_{initial}$, where M_{bound} is the bound mass according to the numerical iterative result described in section 2.3.

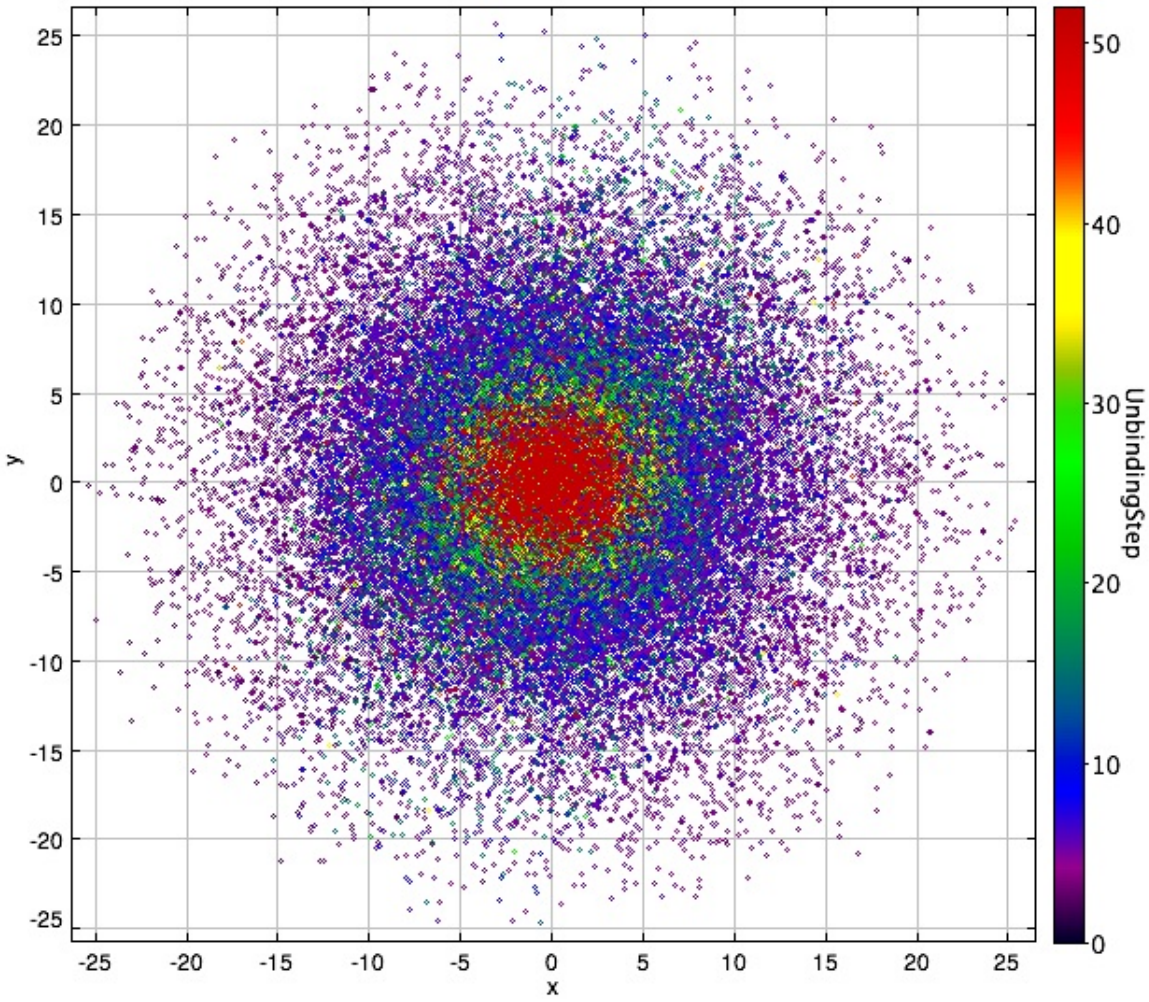

Figure 2.9: Unbinding step of particles, in other words the step at which the energy of the particle becomes positive according to the iterative criterion and results in its unbinding from the satellite. The particles in the core $r < 4$ stay bound to the satellite until the end of the simulation.

Chapter 3

Tidal Model

As the satellite orbits in the host halo it gradually loses mass. The criterion described in section 2.3 gives a numerical measure of this mass loss. In this chapter we want to find an analytic model predicting mass loss based on a few physical phenomena. If we look at figure 2.9 we see that particles getting unbound in each time step of the simulation form almost spherical shells around the satellite's initial mass distribution. Based on this, we may intuitively postulate that in each time step, particles beyond a certain radius get unbound from the satellite due to the gravitational potential of the host halo. As the numerical mass loss criterion is an energy based criterion, this radius should be energy dependent. An approximative approach based on this assumption is the tidal approximation that truncates particles beyond a certain *tidal radius*. This approach is a steady state approximation of mass loss and doesn't take into account structural changes of the satellite due to tidal shocks. Therefore it is not enough to adequately predict mass loss. Heating due to tidal shocks coupled with tidal truncation can more effectively model mass loss. The tidal approximation will be described in section 3.1. An approximative measure of tidal shocks (the impulse approximation) will be studied in section 3.2. The effect of virialization will be described in section 3.3.

3.1 Tidal Truncation

Astrophysical objects such as globular clusters have been observed to have sharp edges. At first sight this might seem in conflict with our expectations. As globular clusters pass through the galactic plane we would expect orbital diffusion to erase sharp features in their structure (Binney & Tremaine, 1994). von Hoerner (1957) studied the internal structure of globular clusters and concluded that beyond a "radius of stability" called *tidal radius*, stars are swept away by external forces. The same approach can be taken for our satellite orbiting in the dark matter halo. Particles of the satellite feel tidal forces from the halo. These tidal forces increase the energy of the particles and those passing the tidal radius will have positive energy and will get unbound. Therefore we can truncate the satellite at its tidal radius as it orbits around the host halo. We start by estimating the tidal radius in a simple situation where the host is a point masse at distance R from the satellite. A particle's distance from the center of the satellite is $r \ll R$. The mass of the host is M_{host} and the satellite's mass inside radius r is $M_{sat}(< r)$. The acceleration at the center of the satellite toward the host is GM_{host}/R^2. The same acceleration at the position of the particle is $GM_{host}/(R-r)^2$. The difference of these two accelerations gives the tidal acceleration of the particle due to the host force in an inertial frame centered on the host:

$$a_{tidal} = \frac{GM_{host}}{(R-r)^2} - \frac{GM_{host}}{R^2} = GM_{host}\ \left[\frac{1}{(R-r)^2} - \frac{1}{R^2}\right] \tag{3.1}$$

As $r \ll R$ we can approximate the term in brackets and the tidal acceleration becomes:

$$a_{tidal} \simeq \frac{2\ GM_{host}\ r}{R^3} \tag{3.2}$$

The acceleration of the particle toward the satellite is:

$$a_{sat} = \frac{GM_{sat}(< r)}{r^2} \tag{3.3}$$

The radius at which $a_{tidal} = a_{sat}$ is called the "tidal radius". If the particle passes this radius the tidal force from the host will be greater than the satellite's gravity and the particle will get unbound. From equating 3.2 and 3.3 we can obtain this radius:

$$r_t = R\ \left[0.5\ \frac{M_{sat}(< r_t)}{M_{host}}\right]^{1/3} \tag{3.4}$$

Rearranging equation 3.4 we find:

$$\frac{M_{host}}{R^3} = 0.5 \ \frac{M_{sat}(< r_t)}{r_t^3} \tag{3.5}$$

In other words with a point mass host the tidal radius of the satellite is a place where the average density of the satellite is twice the average density of the host:

$$\bar{\rho}_{sat}(< r_t) = 2 \ \bar{\rho}_{host}(< R) \tag{3.6}$$

This expression of the tidal radius was first found for globular clusters moving towards the galactic plane by von Hoerner (1957).

Now we want to find a more general expression of the tidal radius for a satellite on a circular orbit around a spherically symmetric mass distribution with a given potential $\Phi(R)$. For this we choose our coordinate system to be centered at the center of mass of the satellite and co-rotating with it so that its x-axis points toward the center of the host. The angular velocity of the motion of the coordinate system around the host is Ω. As the orbit is circular Ω is constant. The fact the orbit is circular also implies that the coordinate system needs to self-rotate with the same angular velocity as its orbit for the alignment of its x-axis. In this frame the center of the host halo is at $\vec{R}_{halo}$ and the position of a particle of the satellite is $\vec{r}$. The accelerations of this particle due to the host halo and the satellite are respectively:

$$\vec{a}_{host}(\vec{r}) = -\nabla\Phi(|\vec{R}_{host} - \vec{r}|) \tag{3.7}$$

$$\vec{a}_{sat}(\vec{r}) = -\frac{GM_{sat}(< r)}{r^3} \ \vec{r} \tag{3.8}$$

As the frame is non-inertial its acceleration gives rise to fictitious forces on the particle. The acceleration of the frame's motion relative to an inertial frame such as a static frame at the center of the host halo is:

$$\vec{a}_{frame} = -\nabla\Phi(R_{host}) + \vec{r} \ \Omega^2 \tag{3.9}$$

The tidal radius is where the following equation holds:

$$\vec{a}_{host} - \vec{a}_{sat} = \vec{a}_{frame} \tag{3.10}$$

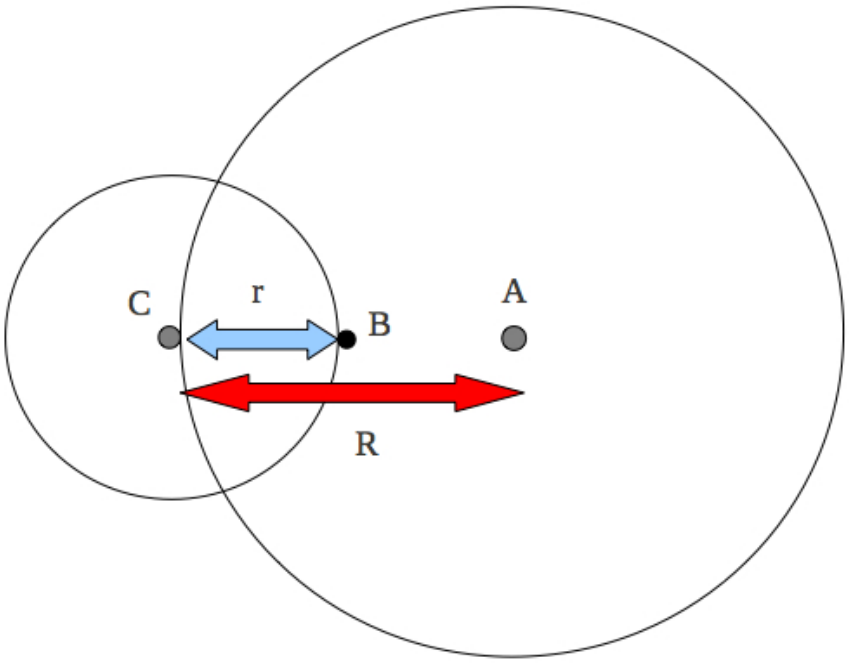

Figure 3.1: Schematic illustration of the satellite centered at point C moving on a circular orbit around the host which is a point mass positioned at A.

Substituting for each of the accelerations we have:

$$-\nabla\Phi(|\vec{R}_{host}-\vec{r}_t|)+\frac{GM_{sat}(<r_t)}{r_t^3}\ \vec{r}_t=-\nabla\Phi(R_{host})+\vec{r}_t\ \Omega^2 \tag{3.11}$$

$$\nabla\Phi(R_{host})-\nabla\Phi(|\vec{R}_{host}-\vec{r}_t|)+\frac{GM_{sat}(<r_t)}{r_t^3}\ \vec{r}_t=\vec{r}_t\ \Omega^2 \tag{3.12}$$

If $r \ll R_{host}$ then we have:

$$\nabla\Phi(R_{host})-\nabla\Phi(|\vec{R}_{host}-\vec{r}_t|)\simeq\frac{d^2\Phi(R)}{dR^2}\Big|_{\vec{r}_t}\ \vec{r}_t \tag{3.13}$$

Therefore equation 3.12 becomes:

$$\frac{d^2\Phi(R)}{dR^2}\Big|_{\vec{r}_t}\ \vec{r}_t+\frac{GM_{sat}(<r_t)}{r_t^3}\ \vec{r}_t=\vec{r}_t\ \Omega^2 \tag{3.14}$$

$$\frac{d^2\Phi(R)}{dR^2}\Big|_{\vec{r}_t}+\frac{GM_{sat}(<r_t)}{r_t^3}=\Omega^2 \tag{3.15}$$

We can find the tidal radius from equation 3.15:

$$r_t = \left[\frac{GM_{sat}(< r_t)}{\Omega^2 - \frac{d^2\Phi(R)}{dR^2}\Big|_{\vec{r}_t}} \right]^{1/3} \tag{3.16}$$

It is interesting to note that if $\Phi(R)$ corresponded to the potential of a point particle $\Phi(R) = -GM/R$, then the orbital velocity around it would be keplerian $\Omega = \sqrt{GM/R^3}$ and $\frac{d^2\Phi(R)}{dR^2} = -2GM/R^3$. Therefore putting these in the above equation and rearranging we would get:

$$\bar{\rho}_{sat}(< r_t) = 3\ \bar{\rho}_{host}(< R) \tag{3.17}$$

Therefore for a circular orbit, the tidal radius happens when the density contrast is 3 rather than 2 as the first situation with two inertial point particles.

To find the general average density contrast at the tidal radius we rearrange equation 3.16:

$$\frac{M_{sat}(< r_t)}{4/3\ \pi\ r_t^3} = \frac{1}{4/3\ \pi\ G} \left[\Omega^2 - \frac{d^2\Phi(R)}{dR^2}\Big|_{\vec{r}_t} \right] \tag{3.18}$$

We define $\Omega_c = \sqrt{GM_{host}/R^3}$ as the angular velocity of a circular orbit of radius R around the host. We can rewrite equation 3.18 as:

$$\frac{M_{sat}(< r_t)}{4/3\ \pi\ r_t^3} = \frac{1}{4/3\ \pi\ G} \left[\frac{\Omega^2}{\Omega_c^2} - \frac{1}{\Omega_c^2}\frac{d^2\Phi(R)}{dR^2}\Big|_{\vec{r}_t} \right] \frac{GM_{host}}{R^3} \tag{3.19}$$

Which can be written as:

$$\bar{\rho}_{sat}(< r_t) = \eta\ \bar{\rho}_{host}(< R) \tag{3.20}$$

Where:

$$\eta = \frac{\Omega^2}{\Omega_c^2} - \frac{1}{\Omega_c^2}\frac{d^2\Phi(R)}{dR^2}\Big|_{\vec{r}_t} \tag{3.21}$$

It is worth noting that $\Omega^2/\Omega_c^2 = L^2/L_c^2 = e^2$ where e is the circularity parameter.

Equation 3.16 gives an approximative expression for the tidal radius. This approximation called the tidal approximation is based on two assumptions: (1) The orbit of the satellite is circular. (2) The satellite is far from the host, $r_{sat} \ll R_{host}$ so that the change

of the gravitational potential of the host halo is small inside the satellite. None of these two assumptions holds for our problem. First our satellite is on an elongated orbit around the host and second it gets close to the center of the halo at pericentral passages.

King (1962) has argued that for elongated orbits the tidal radius just needs to be calculated at the pericenter of the orbit from expression 3.16. From the point mass host example discussed above (equ. 3.4) we saw that $r_t \propto R_{host}$, which means that as we go toward the center of the host halo the tidal radius of the satellite shrinks. This in turn means that the tidal radius will be smallest at the pericenter of the orbit. According to King (1962) the density profile of the satellite should be truncated when the tidal radius is smallest.

Taylor & Babul (2001) suggested a better procedure. They used expression 3.16 as the instantaneous tidal radius of the satellite. They chose the instantaneous angular velocity of the satellite around the host halo as Ω in this expression. They calculated the tidal radii at different positions of the satellite on its orbit. The satellite was truncated instantaneously at each tidal radius. However as mentioned in section 2.3 it takes some time for the energy of each particle that passes through the tidal radius to become positive. This timescale is of the order of the orbital period of the satellite around the host. Taylor & Babul (2001) assumed that the satellite mass beyond the tidal radius is lost over the course of one orbital period, and scaled the mass loss accordingly.

Here I adopt the same procedure. I calculate the instantaneous tidal radii of the satellite for 50 time steps on its orbit using equ. 3.16. The angular velocity in this equation will be $\Omega_{inst} = v_{perp}/R_{host}$ (the perpendicular component of the velocity of the center of mass of the satellite divided by the distance of the center of mass to the center of the host halo). The second derivative of the potential of the host halo will be calculated at the center of mass of the satellite using the analytic expression of the NFW potential (equ. 2.9). Calculating the potential at the center of mass of the satellite instead of doing so at the tidal radius is valid in the $r_{sat} \ll R_{host}$ limit, which is the limit of validity of the tidal approximation. Figure 3.2 shows this tidal radius versus time step for the parameters of OrbitC. The tidal radius has been scaled by the virial radius of the satellite ($r_{vir} = 16$ in OrbitC). If we use a fixed $M_{sat}(< r_t) = 1$ in equ. 3.16 we will have the solid curve in

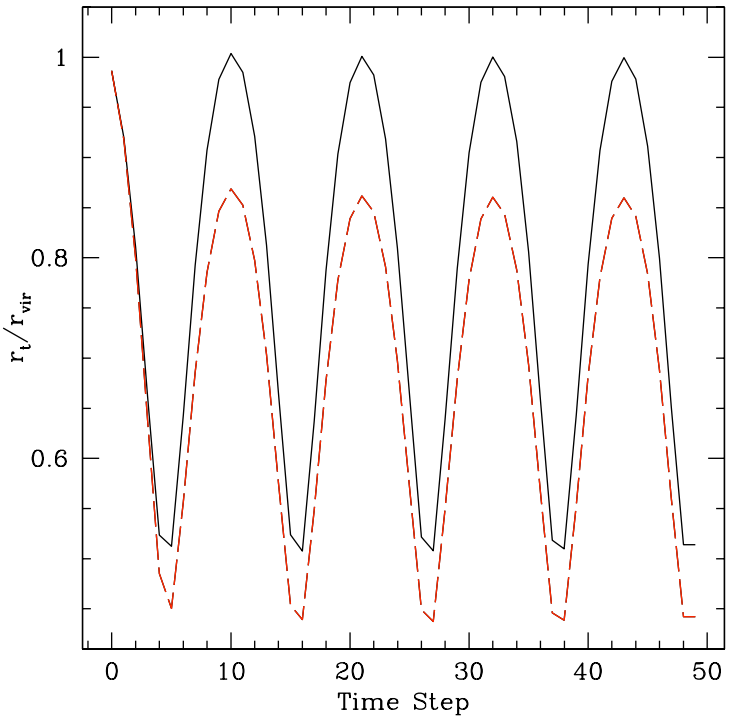

Figure 3.2: The solid curve shows the tidal radius versus time, where the tidal radius is calculated using a fixed $M_{sat}(< r_t) = 1$ in equ. 3.16. The red dashed curve shows the tidal radius versus time, where $M_{sat} = M_{sat}(< r_t)$ of the preceding step in equ. 3.16.

figure 3.2. We see that this tidal radius is equal to the virial radius of the satellite at the beginning when the satellite is at its apocenter (time step=0). This is logical as all the particles are bound in time step zero. Then it goes to its minimum at the first pericentral passage (time step=5), and goes back to its initial apocenter value and oscillates between the maximum and minimum. However if we use a varying $M_{sat}(< r_t)$ in equ. 3.16 (the bound mass of the preceding time step calculated using $M_{NFW}(< r_t)$ from equ. 2.3 where r_t is the tidal radius found in the preceding time step) we will have the red dashed curve in figure 3.2. In this case the tidal radius will start by the same value, but will decrease more as the tidal bound mass is now decreasing in equ. 3.16. As a result the tidal radius will oscillate between a lower maximum and minimum. Figure 3.3 illustrates the tidal radius of the satellite as a function of its center of mass distance from the center of the host. As

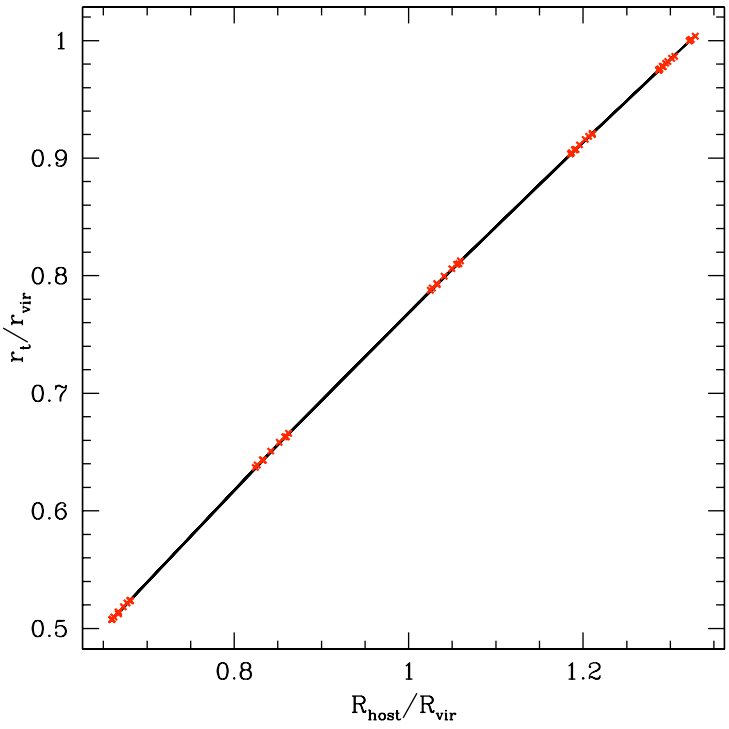

Figure 3.3: Tidal radius versus distance from the center of the host for OrbitC. Both the tidal radius and the distance have been scaled to the virial radii of the satellite and the host halo.

we saw in equ. 3.4, $r_t \propto R_{host}$.

Now that we have the tidal radii in different time steps, we want to predict mass loss. We truncate the NFW mass of the satellite (from equ. 2.3) at each tidal radius and scale this according to the Taylor & Babul (2001) criterion described above. In other words, from the mass beyond the tidal radius in that step we only unbind a fraction dt/T, where dt is the time between two subsequent time steps and T is a measure of the period of the satellite around the host. More precisely, going from step $i-1$ to step i:

$$M_i = M_{i-1} - (\frac{dt}{T}) \times \Big(M_{i-1} - M_{NFW,\,i}\,[\,< r_t\,]\,\Big) \tag{3.22}$$

Where $M_{NFW}(< r_t) = 4\pi\rho_s r_s^3\Big[\ln(1+r_t/r_s) - r_t/(r_s+r_t)\Big]$. We can use different measures for T. Figure 3.4 shows this calculation for four measures of the period (the radial and

azimuthal orbital periods of the satellite defined in appendix A and the instantaneous period calculated as $T_{inst} = 2\pi/\Omega_{inst}$). The solid black curve is the numerical mass loss curve from fig 2.8. The red solid curve is the analytic M_i from the tidal truncation (equ. 3.22). For the red dashed curve, we have looked at the simulation of the satellite in different time steps and unbound particles beyond the tidal radius found from equ. 3.16. Therefore this curve is not completely analytic and has used the particle positions in the simulation. The first conclusion from this plot is that the tidal truncation model alone (red solid curve) predicts less mass loss than the numerical results (solid black) in all cases. The second conclusion is that a fixed orbital period such as the radial or azimuthal orbital periods does not give the correct mass loss curve. More specifically, a fixed orbital period does not reproduce the more rapid mass loss expected at pericenter and the less rapid mass loss expected at apocenter. The third conclusion is that the best measure of the period of the satellite for scaling mass loss in the tidal truncation is half the instantaneous period (bottom right plot in fig. 3.4). With this scaling the tidal approximation predicts tidal radii in an almost exact way (red dashed curve). It also predicts tidal mass loss correctly until the first pericentral passage (time step=5, red solid curve). After that it diverges from the numerical result. This divergence is due to the fact that the steady-state approximation of the tidal truncation model doesn't hold when the satellite is near the center of the host halo. As we shall see tidal shocks become important at pericenter.

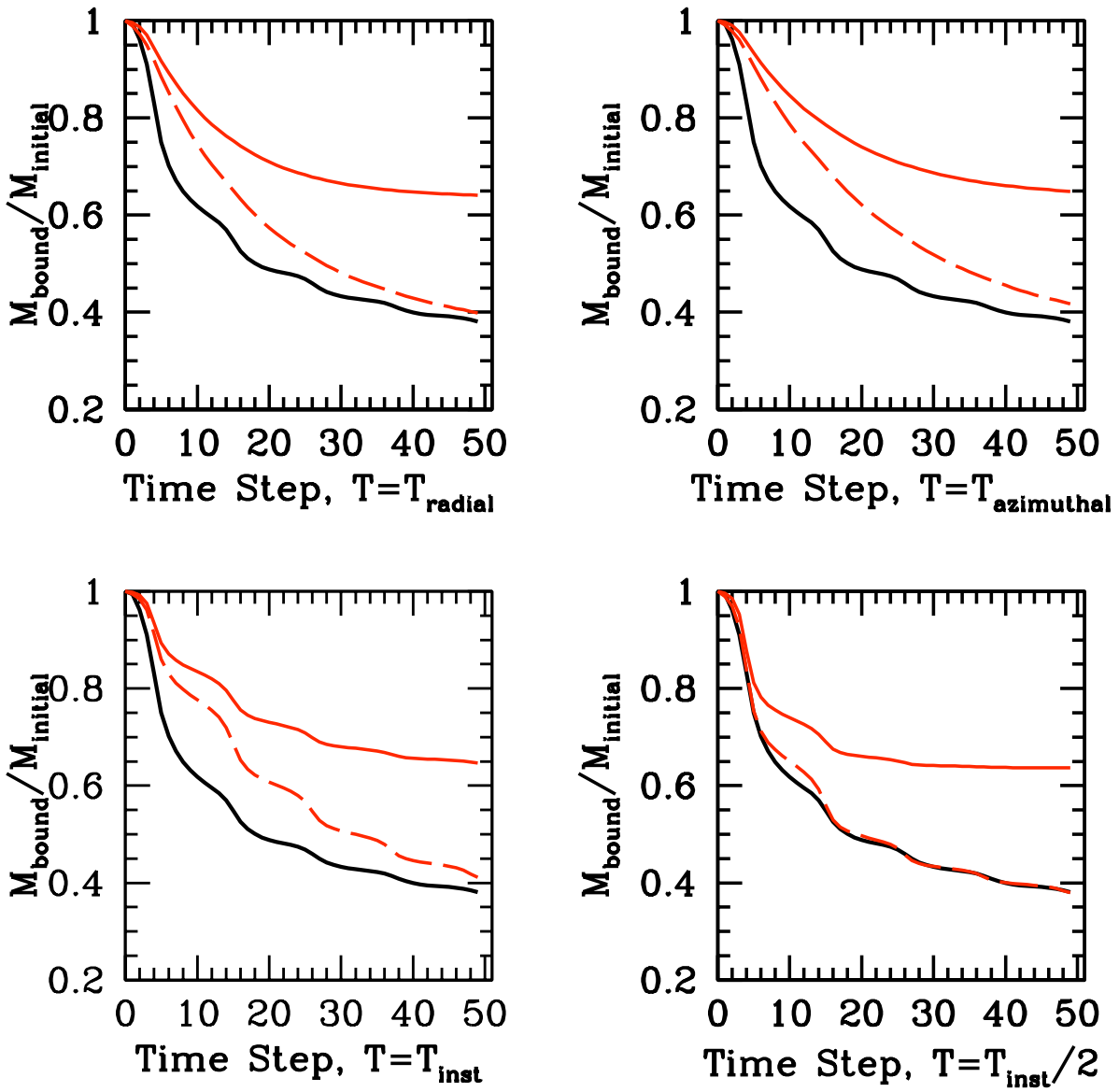

Figure 3.4: Tidal Mass Loss. The solid black curve is the numerical mass loss curve from fig 2.8. The red solid curve is the analytic M_i from the tidal truncation (equ. 3.22). For the red dashed curve, we have looked at the simulation of the satellite in different time steps and unbound particles beyond the tidal radius found from equ. 3.16. In the top figures mass loss has been scaled with constant radial (left) and azimuthal (right) orbital periods. In the bottom figures mass loss has been scaled with the instantaneous orbital period (left) and half this period (right).

3.2 Tidal Shocks

As we saw in the previous section, the tidal truncation model alone can not explain fully the mass loss of the satellite. This is mainly because the tidal approximation is based on the assumption that the distance of the satellite from the host is much bigger than the radius of the satellite. In other words $r_{sat} \ll R_{host}$. This assumption gives rise to a small tidal field that does not change appreciably the velocities of particles in orbit inside the tidal limit of the satellite. Only at the tidal radius, the gravitational potential of the satellite falls below the tidal field and this results in the unbinding of particles and the truncation scheme explained in section 3.1.

However this assumption does not hold everywhere. When the satellite gets close to the pericenter of its orbit the tidal field becomes strong enough to change the velocities of particles inside the tidal limit. Since the duration of this strong tidal field at pericenter is usually much less than the period of the orbit of a typical particle in the satellite this is called a *tidal shock*. Tidal shocks have been first studied in other astrophysical contexts. For instance Spitzer (1958) studied shocks induced by passing interstellar clouds accelerating stars in a galactic cluster and Ostriker et al. (1972) studied the effect of tidal shocks on the evolution of globular clusters. According to these past works in order to calculate the effect of tidal shocks it is useful to make the "impulse approximation".

3.2.1 Impulse Approximation

In order to do a simple calculation to understand tidal shocks we can use the schematic figure 3.1 again. The satellite's center of mass is at a distance R from the center of the host halo. A particle at point B is orbiting in the satellite. This time R is small (the satellite is at its pericenter). If the gravitational field of the host halo is $g(R)$ at the center of the satellite and is $g(R-r)$ at the position of the particle, then the tidal field induced on the particle will be $g(R-r) - g(R)$. This tidal field will change the velocity of the particle so that:

$$\frac{dv}{dt} = \; g(R-r) - g(R) \; \simeq \; r \; \frac{dg(R)}{dR}\Big|_R \tag{3.23}$$

$$\Delta v = \int r \left. \frac{dg(R)}{dR} \right|_R dt \tag{3.24}$$

$$\Delta v = \int r \left. \frac{dg(R)}{dR} \right|_R \frac{dt}{dR} dR \simeq \frac{\Delta g(R)\, r}{V(R)} \tag{3.25}$$

Where $\Delta g(R)$ is the change of the gravitational field of the host at the center of mass of the satellite during the shock period and $V(R)$ is the velocity of the center of mass of the satellite on its orbit around the host. The approximation in equ. 3.25 assumes that the distance of the particle to the center of the satellite r does not change due to the shock; only its velocity changes. In the impulse approximation, the tidal field changes suddenly before the the satellite's structure changes so that each particle experiences an instantaneous change of velocity at a fixed position.

For this assumption to be valid we need:

$$dr \ll r \tag{3.26}$$

$$\frac{dr}{dt} \ll \frac{r}{dt} \;\Rightarrow\; v_r \ll \frac{r}{\Delta R / V(R)} \tag{3.27}$$

Where ΔR is the change of position of the center of mass of the satellite during the shock. In other words the shock is impulsive for particles far from the center of the satellite. As we saw in figure 2.4 the radial velocity dispersion of particles in an NFW profile increases up to the scale radius and then decreases, which means that large radii correspond to long internal periods of the particles. Therefore another way of stating the shock criterion is:

$$t_{shock} \ll t_{orb} \tag{3.28}$$

Where t_{shock} is the time scale of the shock and t_{orb} is the internal orbital period of the particles in the satellite. Taylor & Babul (2001) have chosen $t_{shock} \simeq R/V(R)$ and t_{orb} as the internal orbital period at the half mass radius r_h of an NFW potential with the parameters of our satellite. The authors have also used the following general expression for the tidal acceleration in a Cartesian coordinate frame centered on the center of mass of the satellite:

$$\mathbf{A}_{tid} \;=\; \mathbf{x}(t) \cdot \nabla \mathbf{g} \Big|_{(\mathbf{x}=\mathbf{0})} \;=\; g_{a,b}\; x_b(t)\; \mathbf{e_a} \tag{3.29}$$

Where $\mathbf{x}$ is the position vector in the satellite frame and $g_{a,b} = \partial g_a / \partial X_b$. The X_i are the coordinates in the frame of the host halo. Equation 3.29 is the generalization of equation 3.23. $\nabla \mathbf{g}$ is calculated at the center of mass position of the satellite in equation 3.29. If R is the position of the center of mass of the satellite in the host frame, then as the host has a spherical NFW profile the gravitational force $\mathbf{g}$ is given by:

$$\mathbf{g}(R) = -\frac{GM_{NFW}(< R)}{R^3}\ \vec{R} \tag{3.30}$$

Where from equation 2.3 we have:

$$M_{NFW}(< R) = M_{vir}\ \frac{\ln(1 + R/r_s) - R/(r_s + R)}{\ln(1 + c) - c/(1 + c)} \tag{3.31}$$

M_{vir}, r_s and c are the NFW parameters of the host halo explained in the last chapter. Substituting 3.31 in 3.30 we can write one of the components of $\mathbf{g}$ as:

$$\mathbf{g}_X = -\frac{GM_{vir}}{\ln(1 + c) - c/(1 + c)}\ \frac{\ln(1 + R/r_s) - R/(r_s + R)}{R^3}\ X \tag{3.32}$$

As $R = \sqrt{X^2 + Y^2 + Z^2}$ we can find $\partial g_X / \partial X$, $\partial g_X / \partial Y$ and $\partial g_X / \partial Z$. These calculations are done in Appendix B. Overall we have nine terms for the $g_{a,b} = \partial g_a / \partial X_b$. Substituting these terms in equation 3.29 will give use the tidal acceleration of particles in the satellite.

We want to know how much work this tidal acceleration does on the particles during the shock and how much energy is transfered to the satellite. Assuming the initial velocity of a particle is v, the tidal acceleration will change it to $v + \Delta v$ where Δv is of the order of the expression in equation 3.25 where we have used the impulse approximation. As the impulse approximation assumes that the shock only changes the velocity of particles and not their position, this change of velocity will result only in a change of the kinetic energy. Therefore the energy change per unit mass will be:

$$\Delta E = \Delta K = \frac{1}{2}\ [\ (v + \Delta v)^2 - v^2\ ] \tag{3.33}$$

$$\Delta E = v\ \Delta v\ +\ \frac{1}{2}\ (\Delta v)^2 \tag{3.34}$$

If we average this over all particles, the first term will average to zero because of the different directions of v and we will have:

$$\langle \Delta E \rangle =\ \frac{1}{2}\ \langle (\Delta v)^2 \rangle \tag{3.35}$$

Using the impulsive Δv from equation 3.25 the average change of energy will be of the order of:

$$\langle \Delta E \rangle = \frac{1}{6} \frac{\Delta g^2 \langle r^2 \rangle}{V^2} \tag{3.36}$$

Where the 1/3 factor comes from averaging over the three spatial directions. This shift in energy does not depend on the velocities of particles in the satellite. Kundic & Ostriker (1995) calculated the higher moments of energy change due to tidal shocks and found that the dispersion is large and does depend on the internal velocities of particles. For instance the second moment is:

$$\langle (\Delta E)^2 \rangle = \frac{1}{3} \langle v^2 (\Delta v)^2 \rangle + \frac{1}{4} \langle (\Delta v)^4 \rangle \tag{3.37}$$

Which from Kundic & Ostriker (1995) is of the order of:

$$\langle (\Delta E)^2 \rangle = \frac{1}{9} \frac{\langle v^2 \rangle \Delta g^2 \langle r^2 \rangle}{V^2} + \frac{5}{64} \frac{r^4 \Delta g^4}{V^4} \tag{3.38}$$

The shift in energy and energy dispersion will heat the satellite in pericentral passages. Taylor & Babul (2001) have calculated the average first-order change of energy $\langle \Delta E \rangle$ and have accounted for the higher moments introducing a factor ϵ_h:

$$\mathbf{\Delta E}_{shock} = \epsilon_h \times \langle \Delta E \rangle \tag{3.39}$$

This is useful in our problem as the energy change due to heating can be compared with the actual energy change in the simulation thus the parameter ϵ_h can be adjusted. In order to calculate $\langle \Delta E \rangle$ the authors used the general expression for the tidal acceleration given in equation 3.29 substituting for the nine $g_{a,b}$ terms calculated in Appendix B. They then calculate the change of energy and average it over a sphere of radius r. If the shock is divided into a series of n discrete time steps of length Δt this average change of energy in the time step n is:

$$\langle \Delta E \rangle (t_n \rightarrow t_{n+1}) = \frac{1}{6} r^2 \Delta t^2 \left[2\, g_{a,b}(t_n) \sum_{i=0}^{n-1} g_{a,b}(t_i) + g_{a,b}(t_n) g_{a,b}(t_n) \right] \tag{3.40}$$

For the details of this calculation see Taylor & Babul (2001). This approach is useful in our problem as we want to calculate the effect of shock heating in discrete steps.

3.2.2 Adiabatic Correction

We saw that the impulse approximation successfully predicts the average change of energy as well as its higher moments due to tidal shocks. However the impulse approximation has its limit of validity. The shock criterion 3.28 says that the approximation is valid only for particles with low orbital velocities compared to the orbital velocity of the satellite. For particles with high velocities or short orbital periods we can not use the term tidal shock anymore as the shock time scale is large, and the gravitational potential varies slowly compared to the change of the potential of the particle on its orbit. We know from orbital dynamics that in slowly varying potentials the actions of motion are adiabatically invariant (Binney & Tremaine, 1994). An action is the area of the two dimensional surface of an orbit in phase-space. As for the orbits discussed here the action is proportional to the energy (which is an integral of motion), the energy does not change. Therefore for these types of short-period orbits there will be no heating.

As a result we have to include this effect and shut down heating when the internal orbital periods become comparable or smaller than the shock time scale. This is done by introducing an adiabatic factor $A(x)$ where $x = t_{shock}/t_{orb}$.

$$\mathbf{\Delta E} = A(x) \times \mathbf{\Delta E}_{shock} \tag{3.41}$$

This factor was first calculated by Spitzer (1958). He found that $A(x) = e^{-2x^2}$. This correction imposes an exponential cutoff on heating. However Weinberg (1994) showed that if we think of the gravitational potential of the perturber (the host halo here) as a sum of perturbations in different frequencies, some of those frequencies might resonate with the internal frequencies of the satellite and actually produce heating. Taking this into account, Gnedin & Ostriker (1999) concluded that instead of an exponential cutoff the following less steep adiabatic function is more suitable:

$$A(x) = (1 + x^2)^{-3/2} \tag{3.42}$$

Figure 3.5 is a comparison of this adiabatic correction with the Spitzer correction. Gnedin & Ostriker (1999) have pointed that for detailed simulations the power of the adiabatic

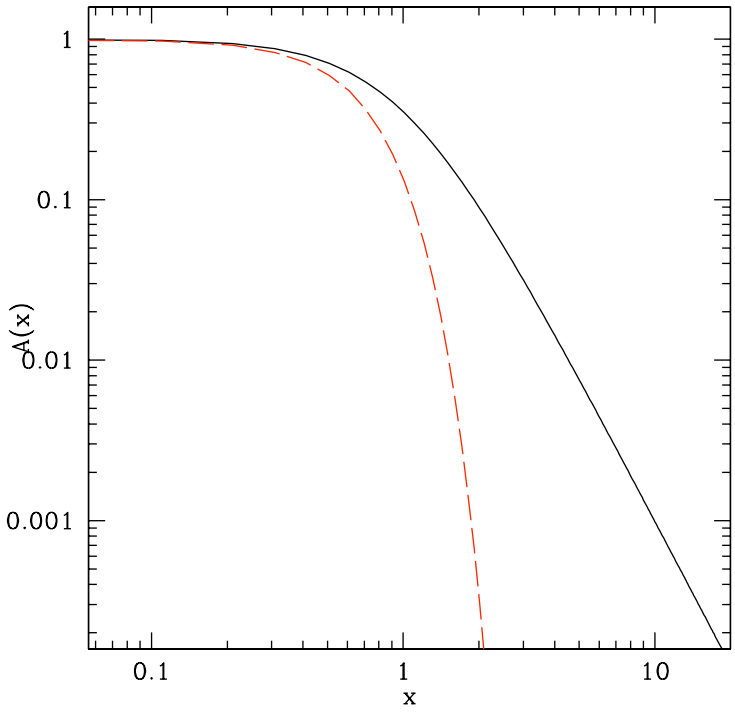

Figure 3.5: Comparison of the Spitzer $A(x) = e^{-2x^2}$ (red dashed) and Weinberg $A(x) = (1+x^2)^{-3/2}$ (solid black) adiabatic corrections.

correction can be adjusted as a free parameter $-\gamma$. This correction $A(x) = (1+x^2)^{-\gamma}$ will have a falling slope somewhere between the Weinberg and Spitzer corrections in figure 3.5.

3.3 Virialization

During the tidal shock an amount of energy $\mathbf{\Delta E}$ is injected in the satellite. This has been corrected adiabatically:

$$\mathbf{\Delta E} = A(x) \times \mathbf{\Delta E}_{shock} \tag{3.43}$$

It also takes into account the higher moments of energy change:

$$\mathbf{\Delta E}_{shock} = \epsilon_h \times \langle \Delta E \rangle \tag{3.44}$$

Where $\langle \Delta E \rangle$ is calculated during the shock using equation 3.40. Therefore the energy change can be summarized as:

$$\mathbf{\Delta E} = A(x) \times \epsilon_h \times \langle \Delta E \rangle \tag{3.45}$$

Now we want to know how this energy affects the satellite. The impulse approximation used in calculating $\langle \Delta E \rangle$ and its higher moments assumed that the tidal field of the satellite only changes the velocities of particles and not their positions. This means that the additional energy is in the form of kinetic energy:

$$\mathbf{\Delta E} = \langle \Delta K \rangle \tag{3.46}$$

We know that for a physical system to remain stable it has to redistribute its energies in a way that satisfies the virial theorem. In other words:

$$-2 \langle K \rangle = \langle P \rangle \tag{3.47}$$

If we assume that the satellite was in virial equilibrium before the shock and evolves to virialize after the shock we will have:

$$\langle E_2 \rangle = \langle E_1 \rangle + \mathbf{\Delta E} = \langle K_1 \rangle + \langle P_1 \rangle + \mathbf{\Delta E} \tag{3.48}$$

$$-2 \langle K_1 \rangle = \langle P_1 \rangle \tag{3.49}$$

Therefore:

$$\langle E_2 \rangle = 0.5 \langle P_1 \rangle + \mathbf{\Delta E} \tag{3.50}$$

The virialization of the satellite gives us:

$$\langle E_2 \rangle = \langle K_2 \rangle + \langle P_2 \rangle = 0.5 \langle P_2 \rangle \tag{3.51}$$

Equating 3.50 and 3.51 we will have:

$$\langle \Delta P \rangle = 2 \mathbf{\Delta E} \tag{3.52}$$

This is the magic of virialization! We started by giving particles kicks in kinetic energy with the average $\langle \Delta K \rangle$, and the satellite redistributes its orbits in phase space in a way that results in two times that change in potential energy.

This change of potential energy can be interpreted in two ways. The first one can relate it to a decrease in the binding energy and gravitational potential of the satellite due to the unbinding of its particles at the shock. The second interpretation is the expansion of the satellite due to heating. We will see in the next chapter that this really corresponds to an expansion. If we assume the satellite expands in a way that particles move from position r to $r + dr$ and the sphere contains mass M, the potential energy change will be:

$$d\phi \;\propto\; d\,(\frac{M}{r}) \;\propto\; \frac{M}{r^2}\,dr \tag{3.53}$$

We assume we do not have shell crossings so that M does not change. The way average density changes in this type of expansion is:

$$d\bar{\rho} \;\propto\; d\,(\frac{M}{r^3}) \;\propto\; \frac{M}{r^4}\,dr \tag{3.54}$$

Therefore:

$$d\bar{\rho} \propto (1/r^2)\; d\phi \tag{3.55}$$

We saw in equation 3.52 that because of virializaton the change of potential energy is proportional to the change of energy due to heating, therefore:

$$\Delta\bar{\rho} \propto (1/r^2)\; \mathbf{\Delta E} \tag{3.56}$$

$$\Delta\bar{\rho} \propto (1/r^2)\; A(x)\; \epsilon_h\; \langle \Delta E \rangle \tag{3.57}$$

From 3.40 we see that $\langle \Delta E \rangle \propto r^2$. As a result $\Delta\bar{\rho}$ will not have an explicit radial dependence. If we use 3.40 to substitute for $\langle \Delta E \rangle$:

$$\Delta\bar{\rho} \propto \frac{1}{6}\; A(x)\; \epsilon_h\;\; \Delta t^2 \left[2\, g_{a,b}(t_n) \sum_{i=0}^{n-1} g_{a,b}(t_i) + g_{a,b}(t_n) g_{a,b}(t_n) \right] \tag{3.58}$$

There is still an implicit dependence on radius in $A(x)$. We know that the adiabatic correction truncates toward the center of the satellite where orbital periods are shorter than the shock time scale. In modeling mass loss we will use an average adiabatic correction $A(\bar{x})$ where $\bar{x}$ is the orbital period at the half mass radius of the satellite over the shock time scale. This new correction will have a similar effect, this time without a radial dependence.

Equation 3.58 gives us a constant shift in density over all radii at the shock. We will have a closer look at average density changes in the the next chapter.

A satellite expanded in the above fashion will have a smaller tidal radius, and therefore will lose more mass than in the steady-state regime. In the next chapter we will see how we can use this tidal model to effectively predict mass loss.

Chapter 4

Evolution of Substructure

In the last chapter we saw that two processes should be taken into account when studying the satellite's evolution: (1) *Tidal truncation*, where all matter beyond a tidal radius gets unbound in a time scale of the order of half the orbital period of the satellite around the host; and (2) *Tidal shocks* at pericentral passages of the satellite that heat it and make it expand. This expansion will decrease the tidal radius resulting in more mass loss. It will also affect the structure of the satellite.

To use the tidal model to predict mass loss, we will do the following: We will use the tidal approximation to truncate the satellite throughout its evolution in the host system. During shocks, we will calculate a smaller tidal radius based on the change of density of the satellite due to heating described in the previous chapter. Then we will truncate the mass of the satellite at those tidal radii. This results in a very accurate prediction of mass loss. We will spend the remaining of the chapter investigating how the structure of the satellite evolves and how this can explain the success of the tidal model.

The time scale of mass loss, T in equation 3.22 is one of the parameters of the problem. It affects the amount of mass lost beyond the tidal radius. It can be readjusted. However we prefer to keep the value of T found when applying tidal truncation to the satellite (figure 3.4) as that successfully predicted the tidal limit of the satellite given by the simulations. This value was half the instantaneous orbital period of the satellite around the host halo.

The tidal model's prediction of heating and the change of density of the satellite during shock (equation 3.58) has two free parameters that need to be adjusted: (1) The heating parameter, ϵ_h is the signature of two main phenomena. First the fact that it accounts for the higher moments of energy change. As we saw in section 3.3 the actual change of potential energy that in turn results in density change is higher than the amount of heating at least by a factor of two due to the virialization of the satellite. We will also account for this in the heating parameter ϵ_h. (2) The power of the adiabatic correction, $-\gamma$ needs to be chosen as its value is somewhere between the Spitzer and Weinberg corrections. From previous studies of the adiabatic correction (Gnedin & Ostriker, 1999; Taylor & Babul, 2001) we choose $\gamma = 2.5$. This will be a suitable choice for predicting the amount of heating. The heating parameter ϵ_h will be adjusted comparing the model with the numerical results of OrbitC. We will then see whether these parameters are correct by using the model to predict the mass loss of OrbitE.

4.1 Model Parameters

To adjust the heating parameter ϵ_h, we calculate the energy change due to heating and adjust it to agree with the actual change of energy of the satellite calculated from the simulation data of OrbitC. To calculate the latter, in each time step of the simulation we choose the particles that are bound to the satellite according to the iterative criterion described in section 2.3 plus the ones that have got unbound in that time step. Then we subtract the orbital energy of the center of mass of the satellite from the energies of each of these particles found in the frame of reference of the host halo and calculate the change of the total bound energy of the satellite in that time step. We do not find the energies of particles by simply adding their kinetic and potential energies in the frame of reference of the satellite because this frame in non-inertial and does not conserve energy.

The change of energy due to heating is calculated only in shock periods. The criterion for the shock is:

$$t_{shock}/t_{orb} < 1 \tag{4.1}$$

Where $T_{shock} = R_{com}/V_{com}$ is the ratio of the distance of the center of mass of the satellite

to the the center of the host halo to its orbital velocity. T_{orb} is the internal orbital period of the satellite calculated at its half mass radius. The value of the half mass radius of the satellite depends on how one defines the bound mass of the satellite. The bound mass of the satellite itself needs to be found after adjusting the heating parameter and predicting the amount of mass loss of the satellite. Therefore we initially find the half mass radius at the first step of the simulation. We use this value to adjust heating. We then predict mass loss. This gives a measure of the bound mass of the satellite in each time step, therefore we can find the correct values of the half mass radius at different steps. Then using these half mass radii gives a better adjustment of the heating parameters. This kind of iteration can be avoided if we use the measure of bound mass from the numerical criterion to find the half mass radius and adjust the heating parameter. The shock criterion turns on heating close to the pericenter and turns it off everywhere else. The heating is calculated using equation 3.40 with Δt being the duration of our time steps and $r = r_h$ the half mass radius of the satellite.

Figure 4.1 shows the energy change of the satellite given by numerical results (black solid curve) and the heating predicted by the tidal shock model (red dashed curve). As we see, most of the heating happens at the first pericentral passage (time step = 5). There are two small peaks at the second pericentral passage (time step $\simeq$ 15). The shocking criterion turns off heating during other parts of the orbit. I have adjusted the parameter ϵ_h to the value below by fitting the first peak in energy change and heating.

$$\epsilon_h = 3.4 \tag{4.2}$$

This value of ϵ_h is higher than the value expected from Gnedin & Ostriker (1997) (ϵ_h=2.33) and is closer to the value used by Taylor & Babul (2001) (ϵ_h=3).

The reason why the the predicted heating does not match the energy change very well after the first peak is due to our approximative shock criterion. We assume that either the whole satellite is under shock (when $t_{shock} < t_{orb}$ where t_{orb} is found at the half mass radius of the satellite) or it is not. This assumption predicts heating at pericenter and predicts zero heating everywhere else. However in reality, a fraction of the particles of the satellite are under shock (when $t_{shock} < t_{i,orb}$ where $t_{i,orb}$ is found for each particle) at each time

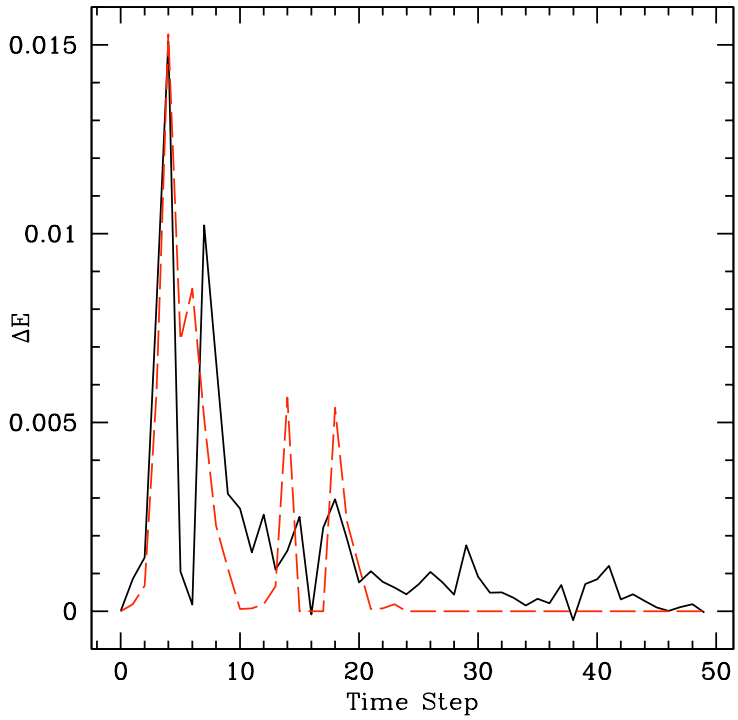

Figure 4.1: Heating ΔE: The black solid curve is the energy change of the satellite given by numerical results and the red dashed curve is the heating predicted by the tidal model.

step. Therefore we will have a net energy change in different steps of the simulation. This net energy change will be highest at pericenter.

4.2 Mass Loss Revisited

Now that the parameters are adjusted and the model predicts the amount of heating during shock periods, we can ask how this affects mass loss. If we assume the average density of the satellite changes by an amount $\Delta\bar{\rho}$ given by equation 3.58:

$$\Delta\bar{\rho} = \frac{1}{6}\,(1+x)^{-2.5}\;\epsilon_h\;\;\Delta t^2\left[2\,g_{a,b}(t_n)\sum_{i=0}^{n-1} g_{a,b}(t_i) + g_{a,b}(t_n)g_{a,b}(t_n)\right] \tag{4.3}$$

where $\epsilon_h = 3.4$ and we put the first cumulative term in brackets equal to zero outside of shock, then we can find a new set of tidal radii based on the new average densities. We saw in section 3.1 that the tidal radius occurs where:

$$\bar{\rho}_{sat}(< r_t) = \eta\ \bar{\rho}_{halo} \tag{4.4}$$

Where:

$$\bar{\rho}_{sat}(< r_t) = \frac{3\ M_{sat}(< r_t)}{4\ \pi\ r_t^3} \tag{4.5}$$

$$\bar{\rho}_{halo}(< r_t) = \frac{3\ M_{NFW}(< R_{com})}{4\ \pi\ R_{com}^3} \tag{4.6}$$

Where R_{com} is the distance of the center of mass of the satellite to the center of the host. η is given by the following expression:

$$\eta = \frac{\omega^2}{\omega_c^2} - \frac{1}{\omega_c^2}\ \frac{d^2\Phi_{host}(r)}{dr^2}\Big|_{R_{com}} \tag{4.7}$$

Where ω_c is the orbital velocity associated with a circular orbit of radius R_{com} around the host, and ω is the instantaneous orbital velocity of the satellite around the host. If we put $\omega_c = \sqrt{(1/R)\ (d\Phi/dR)} = \sqrt{M_{NFW}(< R_{com})/R_{com}^3}$ in the expression for η the tidal radius equation 3.16 is recovered. If we didn't have any expansion then equation 4.4 would be written as:

$$\bar{\rho}_{NFWsat}(< r_t) = \eta\ \bar{\rho}_{halo} \tag{4.8}$$

This would give the tidal radii found in section 3.1 and shown in figure 3.2. If we calculate the average change in density $\Delta\bar{\rho}$ given by 4.3 (where the first cumulative term is set to zero outside of shock) in each time step and add it to the $\Delta\bar{\rho}$ of each of the previous time steps we will find $\Delta\bar{\rho}_{tot}$ of that step, and the above equation becomes:

$$\bar{\rho}_{NFWsat}(< r_m) + \Delta\bar{\rho}_{tot} = \eta\ \bar{\rho}_{halo} \tag{4.9}$$

If we solve this equation for r_m it will give us a set of tidal radii illustrated in figure 4.2 as the red solid curve. These radii are smaller than the previous set of tidal radii found without heating. Now if we truncate the mass of the satellite using equation 3.22 with a scaling of half the orbital period of the satellite we will have a mass loss curve illustrated in figure 4.3. We see that the tidal model agrees remarkably well with numerical results! To

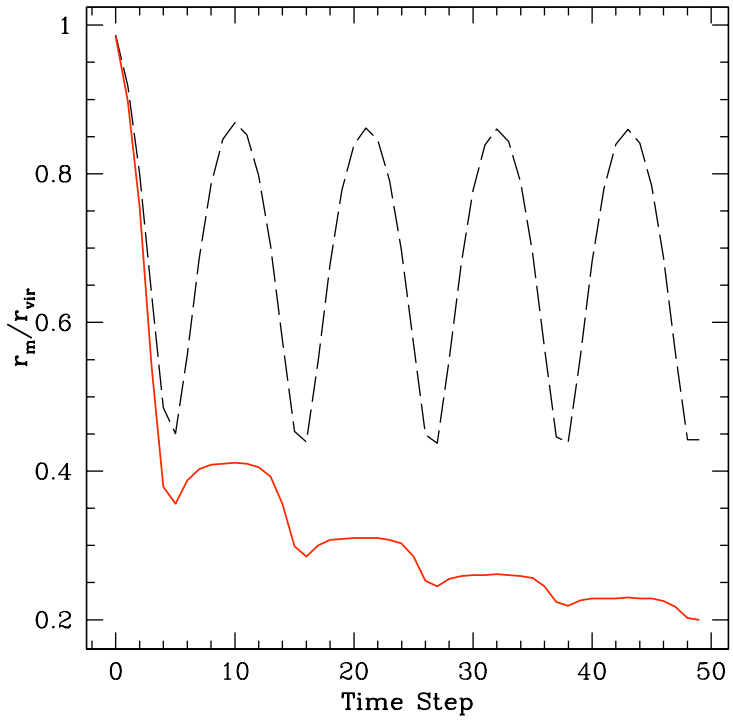

Figure 4.2: New set of tidal radii r_m (red solid curve) calculated with heating included and old set of tidal radii (black dashed curve) versus time step.

test the applicability of the model to other situations we use the same parameters $\epsilon_h = 3.4$ and $\gamma = 2.5$ to apply the tidal model to OrbitE. In OrbitE the satellite is on a more eccentric orbit and gets completely disrupted by tidal forces after 25 time steps. We see in figure 4.4 that the tidal model predicts mass loss to high accuracy in this case too. We conclude that in order to model mass loss analytically we need to take into account the energy change due to heating to first-order. The higher orders will be accounted for by the simple parameter ϵ_h. The updated tidal truncation scheme (taking into account the total average change of density of the satellite due to heating) applied on an NFW density profile will predict mass loss accurately. This prediction is completely analytic whereas the agreement in figure 3.4 (bottom right) used the simulations data.

The density profile of substructures changes due to their expansion caused by heating. This will be inspected in more detail in the following section.

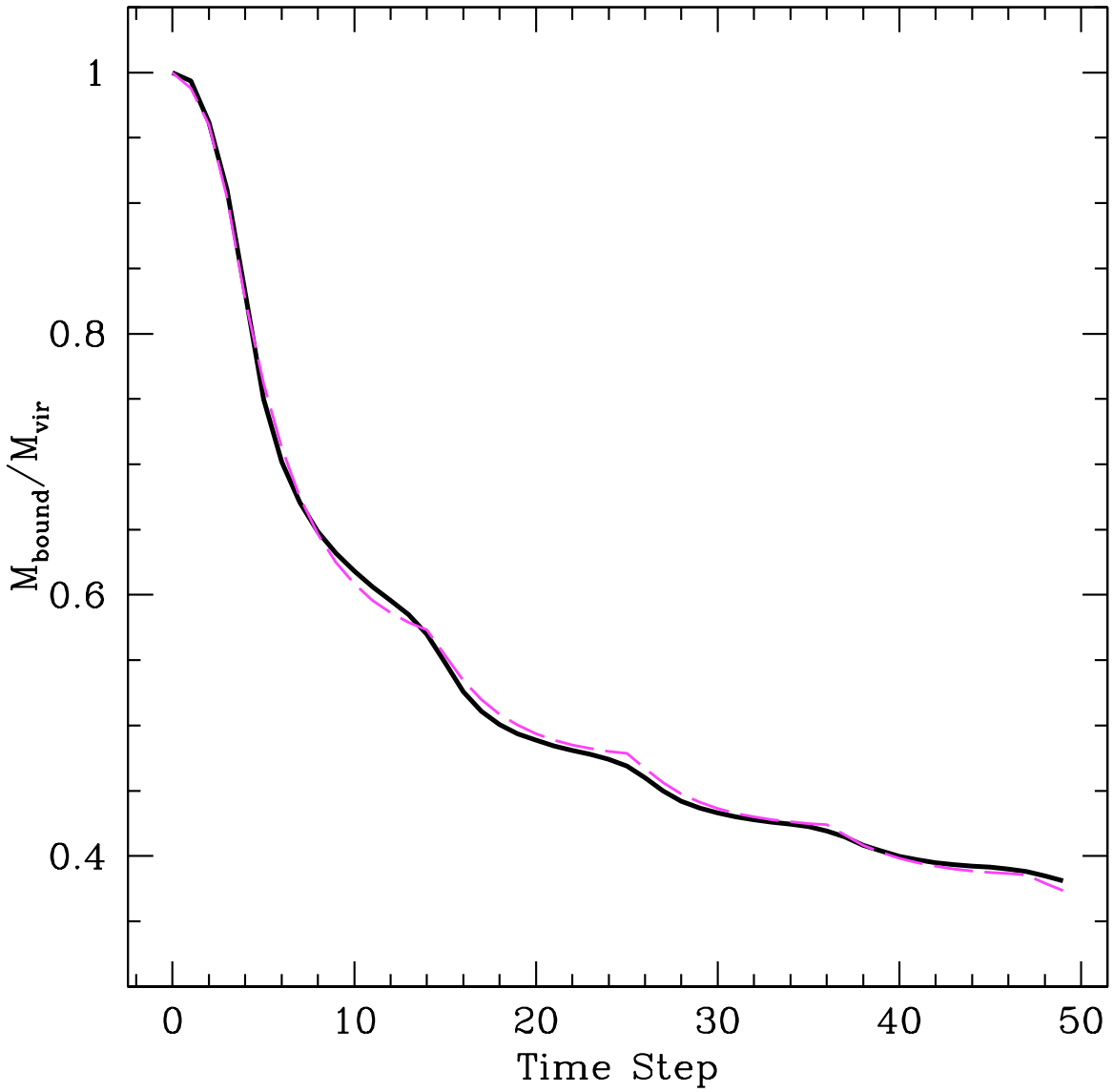

Figure 4.3: Mass loss curve of OrbitC predicted by the tidal model (dashed magenta) agrees very well with the numerical mass loss curve (solid black).

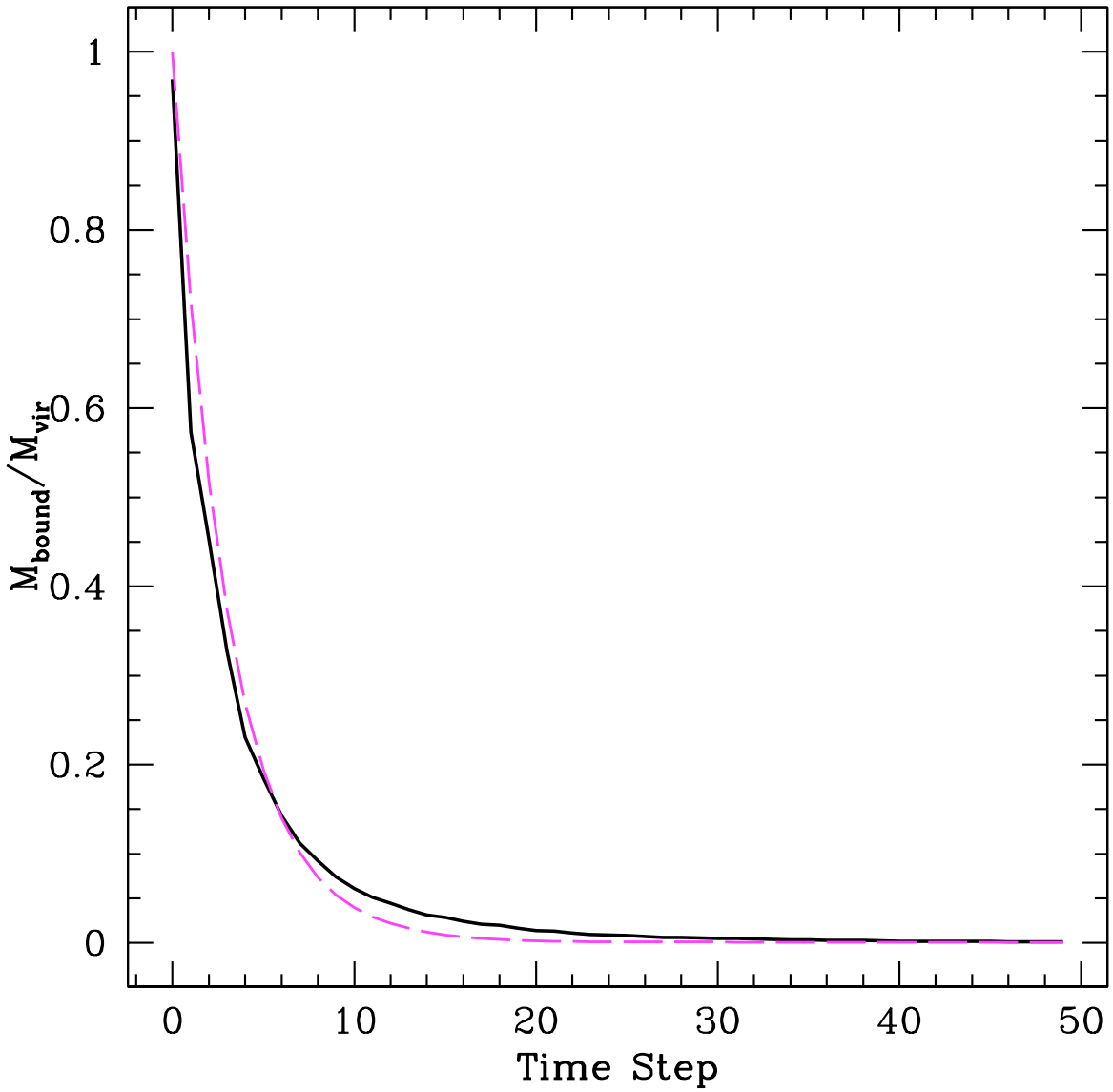

Figure 4.4: Mass loss curve of OrbitE predicted by the tidal model (dashed magenta) agrees with the numerical mass loss curve (solid black).

4.3 Density Evolution

The tidal model predicts mass loss accurately. However, there are a number of questions that need to be answered. One of them is about the truncation method. We have used the new set of tidal radii (solid red in figure 4.2) found by changing the average density of the satellite in the tidal approximation to truncate an NFW profile. How is it that we predict mass loss correctly truncating the unchanged profile? Another question is about the tidal radii themselves. We saw in figure 3.4 (dashed red curve in bottom left figure) that we can correctly calculate the mass loss of the satellite when we unbind the particles of the simulation that fall outside of the old set of tidal radii (r_t) found using the original NFW profile. What is the connection between these two sets of tidal radii?

We can not say that the model is correctly describing the evolution of the satellite without having answered these questions.

4.3.1 Expansion of the Satellite

To see whether the satellite really expands we look at the outer limits of different fractions of its mass in the simulation. This is illustrated in figure 4.5 as well as the two sets of tidal radii r_t and r_m. We see that the satellite's different layers are expanding. We notice three regimes of expansion: (1) Towards the center of the satellite expansion is very slow and almost negligible. (2) Near the new and old tidal radii we have appreciable expansion. (3) Outside the old tidal radius particles are unbound and part of the tidal arms of the satellite stretching in two directions. Thus this latter does not correspond to expansion from heating, but evolution of stripped material.

Using the simulation data, we calculate the densities in different shells at 5 apocenter passages of the satellite. This calculation is carried out for the bound particles of the satellite. These are shown in figure 4.6 with the NFW density profile as the dashed curves. The profiles have been shifted in density for demonstration. We see that at time step = 0 (the first apocenter, top curve in figure 4.6), the satellite's profile is NFW as expected. In the subsequent orbits it starts to diverge from NFW as we go to larger radii. Inside tidal

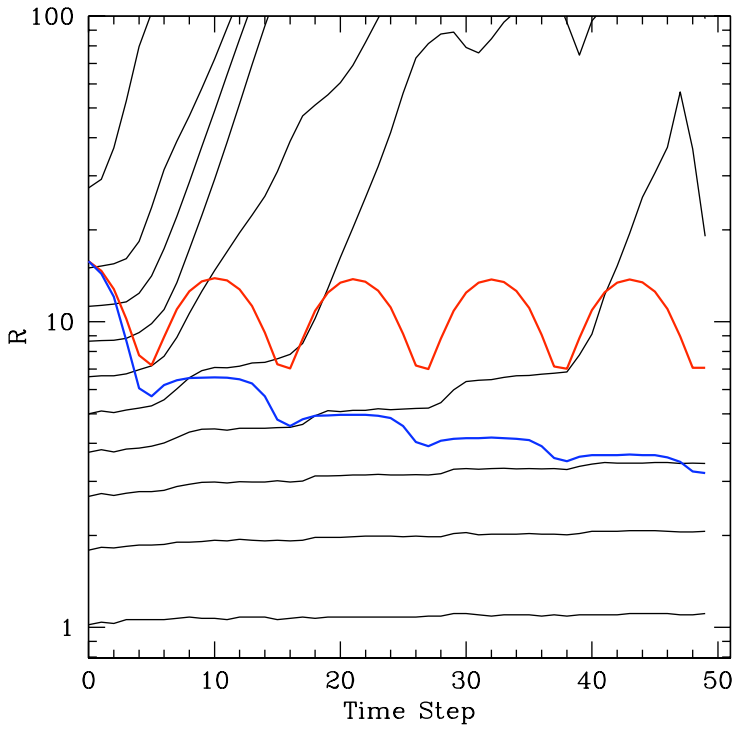

Figure 4.5: From bottom to top the black solid curves show the outer limits of respectively 10, 20, 30, 40, 50, 60, 70, 80, 90 and 100% of the mass of the satellite versus time step. The red curve shows the old tidal radii r_t and the blue curve shows the new tidal radii r_m.

radius r_m (blue points), the deviation is small but outside (red points) the density decreases more rapidly. Hayashi et al. (2003) have studied the evolution of substructure numerically and have found a similar decrease in density in the bound parts of the satellite. The authors have empirically concluded that the following change of the NFW density profile fits the simulation data:

$$\rho(r) = \frac{f_t}{1 + (r/r_{te})^3}\ \rho_{NFW}(r) \tag{4.10}$$

Where f_t and r_{te} are calculated from the bound mass of the satellite using a polynomial fit:

$$\log_{10} r_{te} = 1.02 + 1.38 \log_{10} m_{bnd} + 0.37(\log_{10} m_{bnd})^2 \tag{4.11}$$

$$\log_{10} f_t = -0.007 + 0.35 \log_{10} m_{bnd} + 0.39(\log_{10} m_{bnd})^2 + 0.23(\log_{10} m_{bnd})^3 \tag{4.12}$$

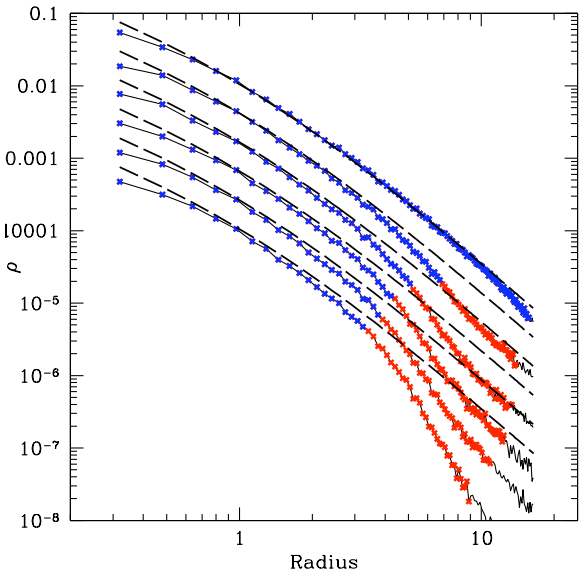

Figure 4.6: Density of the satellite at six apocenter passages calculated for the bound particles compared to the NFW profile (dashed curves). Blue points are inside the new tidal radius r_m and red points inside the old tidal radius r_t.

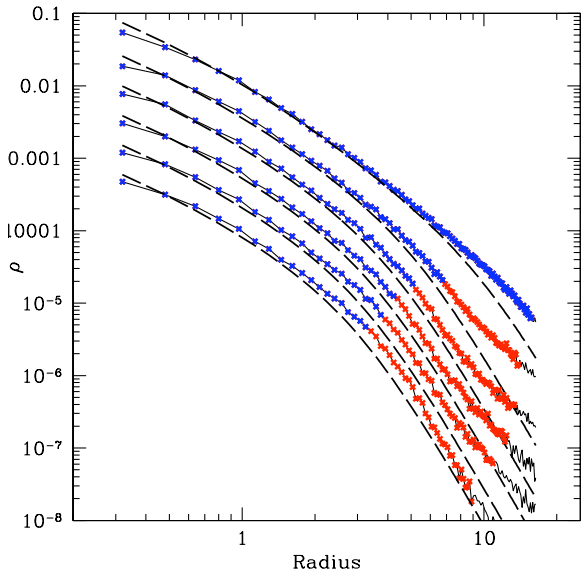

Figure 4.7: Density of the satellite at six apocenter passages calculated for the bound particles compared compared to the Hayashi et al. fit (dashed curves). Blue points are inside the new tidal radius r_m and red points inside the old tidal radius r_t.

This is shown in figure 4.7 as the dashed curves. We see that it fits the density of the satellite well while slightly underestimating it in most radii. This fit depends on the bound mass of the satellite at each time step of the simulation. Thus it can not be considered as an analytic prediction unless it is coupled with a model predicting the bound mass of the satellite. The authors do not explain why the density changes in the above way. They also found that after a few orbits, tides tend to impose a well-defined outer cutoff in the mass distribution of the satellite.

Our results confirm the conclusion of Hayashi et al. (2003) that the satellite's bound structure evolves. This is due to its expansion from heating at pericenter. This expansion is not instantaneous but happens gradually after the pericenter passages of the satellite.

4.3.2 New Density Profile

To find an analytic expression for the new density profile of the satellite, we use a similar functional form as 4.10 but with $f_t = 1$ and $r_{te} = r_m$ (our analytically calculated tidal radius):

$$\rho_{new}(r) \;=\; \frac{1}{1+(r/r_m)^3}\;\rho_{NFW}(r) \tag{4.13}$$

This new density profile is shown in figure 4.8. We see that it agrees with the actual density of the satellite better than the Hayashi et al. (2003) fits shown in figure 4.7. At first the profile is NFW and then it diverges from it. It is now clear why expansion is increased in $r > r_m$ (transition between blue and red in figure 4.8). It is because r/r_m becomes bigger than 1 and as it is to the power of three its effect becomes apparent. On the other hand $(r/r_m)^3$ is close to zero when $r < r_m$. This is why we have an NFW profile close to the center of the satellite. This new density profile also has the advantage of being analytic. The tidal radii r_m can be calculated analytically over the course of the evolution of the satellite.

The evolution of density in the way described by equation 4.13 answers our questions about the validity of the method used to truncate the mass of the satellite. Neither r_m or r_t are the exact tidal radii of the satellite as we have expansion and the steady-state approximation of the tidal truncation method does not hold. The last bound particles lie close to the r_t tidal limit. This is why unbinding particles outside of r_t resulted in a correct mass loss curve (figure 3.4). The expansion of the satellite increases in radii bigger than r_m in a way that results to an outer cut-off in the mass distribution. This is shown in figure 4.9 where the solid black curve is $M_{NFW}(< r)$ and the red dashed curve is $M_{new}(< r) = 4\pi \int_0^r \rho_{new}(r) r^2 dr$ versus r/r_m. We see that the mass of the satellite converges to a value that is equal to the mass of an NFW profile at the tidal radius r_m. As a result we can choose the new set of tidal radii r_m to truncate the NFW density profile.

Kazantzidis et al. (2004b) have concluded that the central profile of substructures can be well fitted with a power-law central slope that is unmodified by tidal forces even after the tidal stripping of 99% of the initial mass and the outer parts can be truncated exponentially. We see from 4.9 that this would be a sensible approximation to the behavior of the satellite.

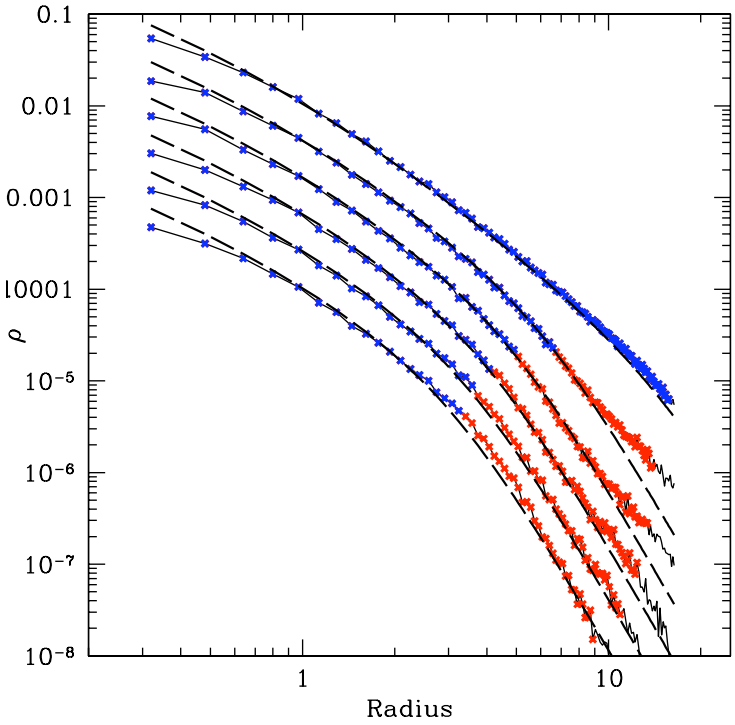

Figure 4.8: Density of the satellite at six apocenter passages compared to the density profile of equation 4.13 (dashed curves). Blue points are inside the new tidal radius r_m and red points inside the old tidal radius r_t.

This behavior is more accurately predicted by the tidal model.

Figure 4.10 shows a comparison of the average densities of the NFW profile and the updated density profile of the satellite (given by equation 4.13) at the 10th time step of the evolution of the satellite when $r_m \simeq 6.5$.

$$\bar{\rho}_{new} = \frac{M_{new}(< r)}{4/3\ \pi\ r^3} = \frac{\int_0^r \rho_{new}(r') r'^2 dr'}{r^3/3} \tag{4.14}$$

We see that they differ by roughly a constant $\Delta\bar{\rho}$ in radii between r_m and r_t. This means that the assumption of the tidal model that heating gives rise to an average density change that is constant with radius is roughly correct in regions between the two sets of tidal radii found with and without heating.

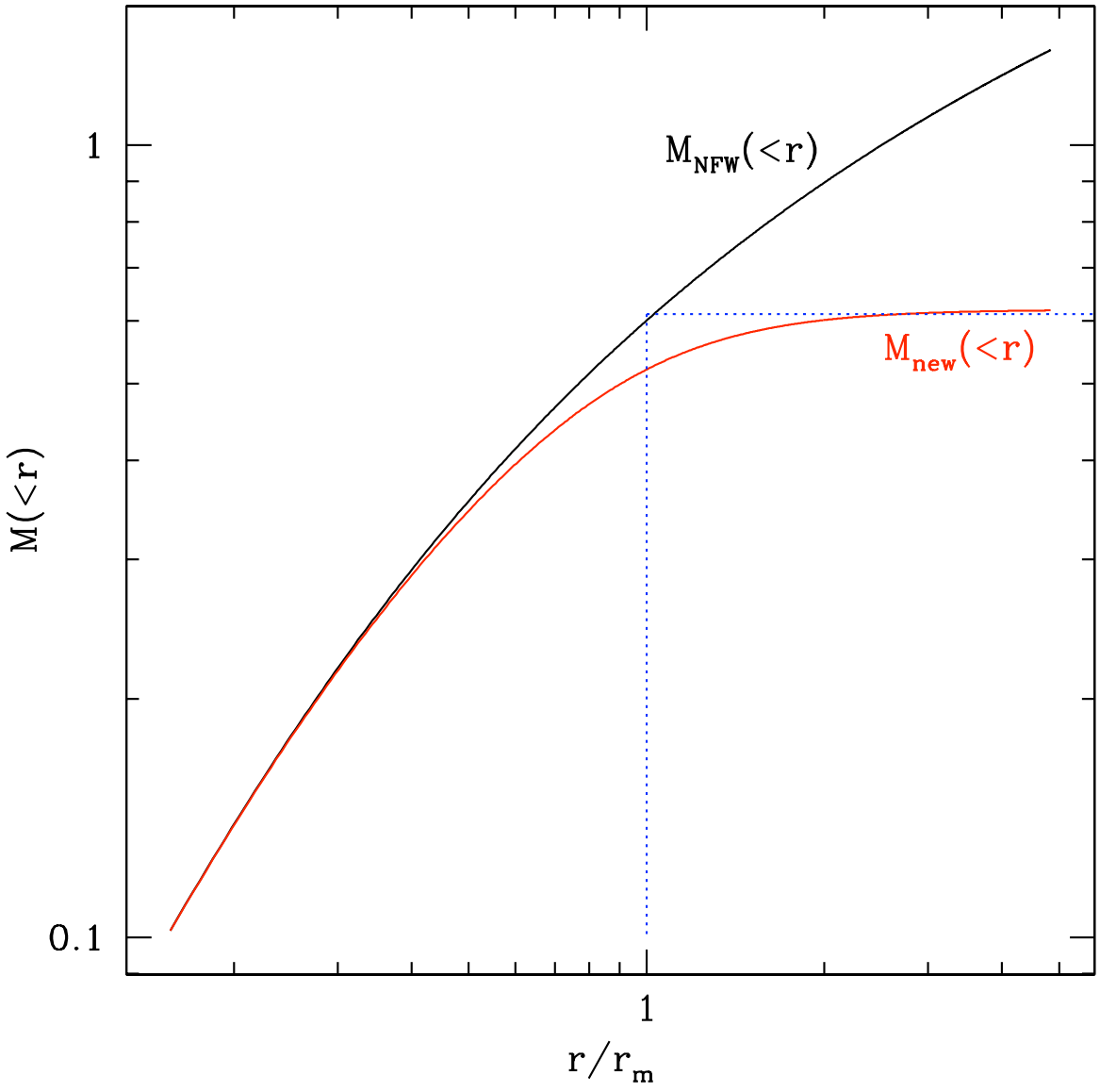

Figure 4.9: Mass of new profile compared to NFW. The solid black curve is $M_{NFW}(< r)$ versus r/r_m and the red curve is $M_{new}(< r)$ versus r/r_m. The mass has been found at the 10th time step of the simulation where $r_m = 6.5$ in units of $r_s = 1$.

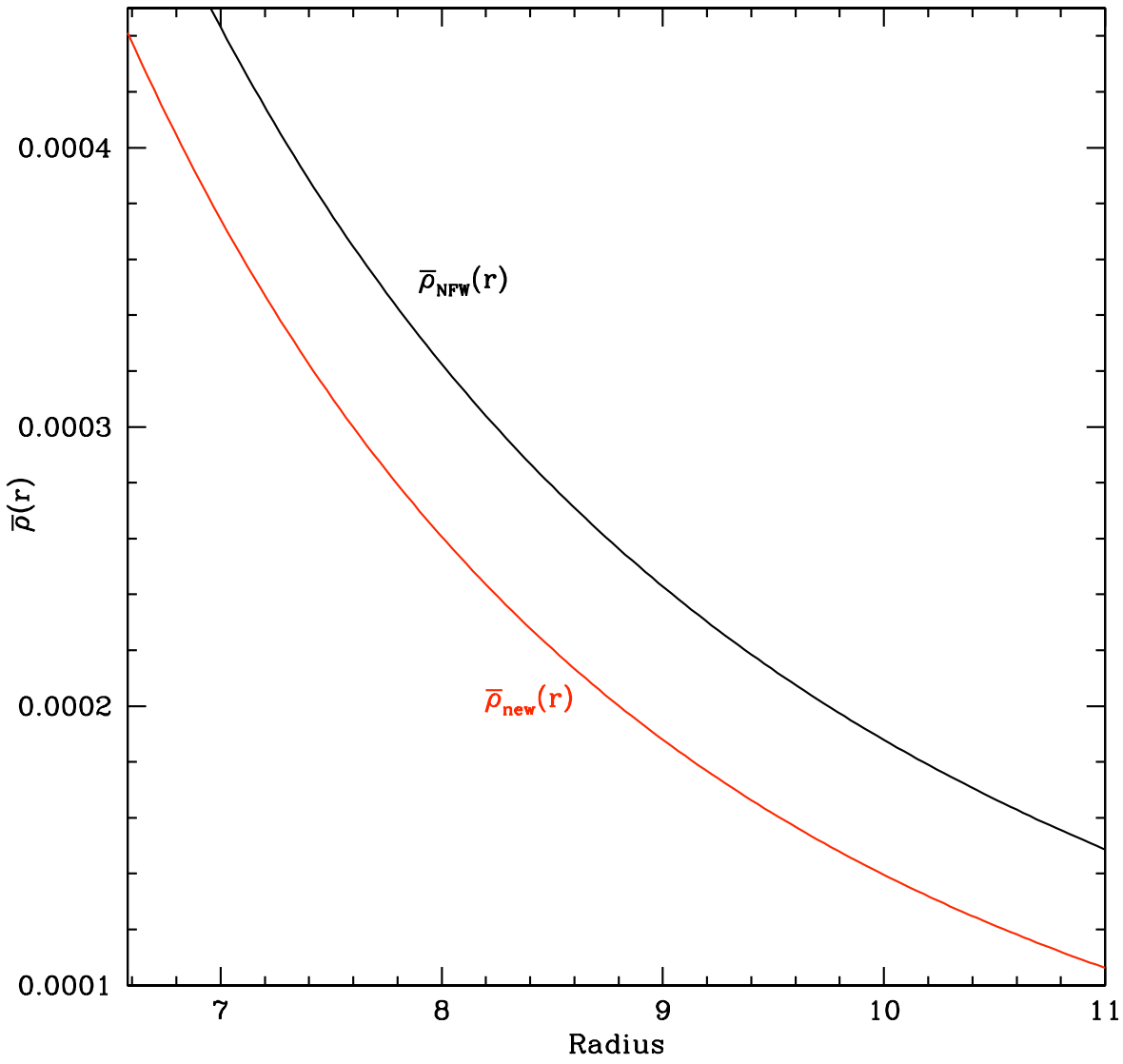

Figure 4.10: Average density of new profile compared to NFW. The solid black curve is $\bar{\rho}_{NFW}(r)$ versus radius and the red curve is $\bar{\rho}_{new}(r)$ versus radius. The average density has been found at the 10th time step of the simulation where $r_m = 6.5$ in units of $r_s = 1$.

Chapter 5

Relaxation

The tidal model successfully describes the evolution of the satellite in the dark matter halo. It explains how the density profile of substructures changes and how they lose mass. It predicts whether a structure with given initial conditions gets disrupted by the tides of its host or stays bound in the course of its evolution. These predictions are particularly useful when cosmological simulations are helpless. We know from the hierarchical nature of structure formation that the structures in the smallest scales were formed early in the history of the universe when the density was higher. In cosmological simulations due to resolution limits each of these dense substructures only has a few particles. This in turn means that each particle of satellites in those simulations is much more massive than candidates for the dark matter particle. When particles are massive they affect each other's velocity. Thus the energy of the particles changes due to their gravitational interactions. As real dark matter particles are collisionless this effect is artificial and might result in the unbinding of particles from the satellite and the artificial disruption of substructures in cosmological simulations. Therefore an analytic model predicting the evolution of substructures in minor mergers is necessary. To investigate how the "artificial relaxation" of particles can affect the evolution of substructures, the same simulations of chapter 2 were run with lower resolutions (N=40000, 10000, 4000, 1000, 400 and 100). Figure 5.2 shows numerical mass loss curves for resolutions N=1h, 4h, 1k, 4k, 10k and 40k (where "h" stands for 100 and "k" for 1000). Our highest resolution N=100k that has been

used so far in the thesis is shown as the black solid curve. We see that when the resolution is lower than 4k the mass loss curve starts to diverge from the correct result. The difference is particularly large for our lowest resolutions 1h and 4h where the satellite is completely disrupted before the 30th time step of the simulation. These precocious disruptions are due to artificial effects in low resolutions.

One way of explaining this is that as we go to lower resolutions particles of the satellite get more massive and affect the velocities of other particles in a way the original dark matter particles don't. To calculate this effect let's consider the following situation illustrated in figure 5.1:

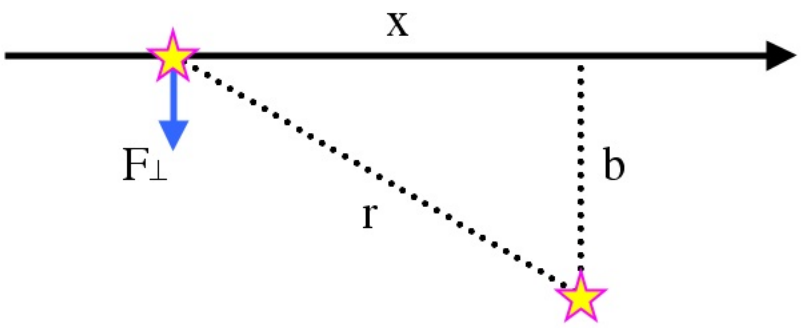

Figure 5.1: Trajectory of a Particle. The particle moves along a trajectory approximated by the solid line. Another particle in vertical distance b from this trajectory exerts a perpendicular force on the initial particle that results in its change of velocity.

Binney & Tremaine (1994) have calculated the perpendicular change of the velocity of one particle due to the gravitational force of the other assuming that the change of velocity is small compared to the initial velocity in a way that does not change the shape of the trajectory. The resulting change of velocity is:

$$|\delta v| \simeq \frac{2\ G\ m}{b\ v} \tag{5.1}$$

If the surface density of particles in the satellite is of order $N/\pi b_{max}^2$ where b_{max} is the largest scale of the system chosen as about 10 times the inter-particle distance by Diemand et al. (2004), then in one crossing the particle will have

$$n = \frac{N}{\pi\ b_{max}^2}\ 2\pi b\ db = \frac{2N}{b_{max}^2}\ b\ db \tag{5.2}$$

encounters with particles in distances between b and db. As the changes of velocity are random $\langle \delta v \rangle$=0, but we will have:

$$\langle \delta v^2 \rangle = n \ |\delta v|^2 = (\frac{2 \ G \ m}{b \ v})^{\ 2} \ \frac{2N}{b_{max}^2} \ b \ db \tag{5.3}$$

Therefore:

$$\langle \Delta v^2 \rangle = \int_{b_{min}}^{b_{max}} \langle \delta v^2 \rangle \ \simeq \ 8 \ N \ (\frac{G \ m}{b_{max} \ \sqrt{\langle v^2 \rangle}})^2 \ \ln \Lambda \tag{5.4}$$

Where $b_{min} \equiv \max(Gm/3\sigma^2, \epsilon)$ and $\Lambda \equiv b_{max}/b_{min}$. The term $b_0 = Gm/3\sigma^2$ is the impact parameter where the deflection angle reaches $\pi/2$ and ϵ is the softening length. The expression above is an approximation as we have assumed that the surface density of particles is constant with radius. However the surface density of particles changes with radius based on the density profile of the satellite. Diemand et al. (2004) have used the term below instead of $\ln \Lambda$:

$$C \equiv 0.5 \ \Big[\ \ln(1 + \Lambda^2) - \frac{\Lambda^2}{1 + \Lambda^2} \ \Big] \quad (\simeq \ln \Lambda, \ \Lambda \gg 1) \tag{5.5}$$

This gives a better approximation to the above integral and accounts for the density changes. The time scale needed for the velocity of particles to change of the order itself is given by:

$$t_{relax} = \frac{\langle v^2 \rangle}{\langle \Delta v^2 \rangle} \times t_{cross} \simeq \frac{3 \ \sigma^2}{\langle \Delta v^2 \rangle} \times t_{cross} \tag{5.6}$$

Where $\sigma^2 \simeq \langle v^2 \rangle / 3$ and the crossing time is of order $t_{cross} \simeq b_{max}/\sqrt{\langle v^2 \rangle} = b_{max}\sqrt{\langle v^2 \rangle}/\langle v^2 \rangle = b_{max}\sigma/3\langle v^2 \rangle$. Therefore:

$$t_{relax} \simeq \frac{\sigma^3 \ b_{max}}{\langle v^2 \rangle \ \langle \Delta v^2 \rangle} \tag{5.7}$$

If we assume the satellite is in virial equilibrium, in other words $\langle v^2 \rangle \simeq \frac{GNm}{b_{max}}$ and if we use equation 5.4 then:

$$t_{relax} \simeq \frac{\sigma^3 \ b_{max}^3}{8 \ G^2 \ m^2 \ N \ C} = \frac{\sigma^3}{8 \ G^2 \ m \ \bar{\rho} \ C} \tag{5.8}$$

Where $\bar{\rho} \simeq Nm/{b_{max}}^3$. Now if we want to use the local density in the above equation, then we have to change the factor in the equation to the one used by Diemand et al. (2004):

$$t_{relax} \simeq 0.17 \ \frac{\sigma^3}{G^2 \ m \ \rho \ C} \tag{5.9}$$

Therefore each particle will have a relaxation time scale given by the above equation in each time step of the simulation. As we want to know how relaxed particles become in the course of the evolution of the satellite we define the number of relaxation crossings of each particle as:

$$N_{relax}(step) \equiv \sum_{i=0}^{step} \frac{\Delta t}{t_{relax}(i)} \tag{5.10}$$

Where Δt is the duration of each time step. This gives an estimate of how much a particle is relaxed. N_{relax} is plotted versus radius in figure 5.3 for the resolutions N = 100k and N= 4h. It has been calculated for each bound particle (black points) at the 10th time step of the simulation. The red points are N_{relax} for the particles that have got unbound in that particular time step. We see that in the high resolution simulation the particles getting unbound have less than one relaxation crossing whereas the particles getting unbound in the lower resolution simulation have more than one relaxation crossing.

Figure 5.4 shows the average number of relaxation crossings of unbound particles versus time step for different resolutions. This average is calculated over particles getting unbound in that particular time step of the simulation (the red points in figure 5.3). We see that in the high resolution simulations (100k, 40k and 10k) stripped particles have less than one relaxation crossing throughout the evolution of the satellite. In average, $N_{relax} > 1$ for stripped particles throughout the evolution of the satellite for resolutions 1k, 4h and 1h. For resolutions 1k and 4h N_{relax} has its highest values near time step 9. If we look at figure 5.2 we see that this is where the mass loss curves of resolutions 1k and 4h are beginning to diverge from the correct curve. The relaxation is dramatic in the lowest resolution 1h where stripped particles soon reach values close to 25 relaxation crossings.

We conclude that artificial relaxation may cause the disruption of substructures in simulations with low resolution where satellites have less than $\simeq 1000$ particles.

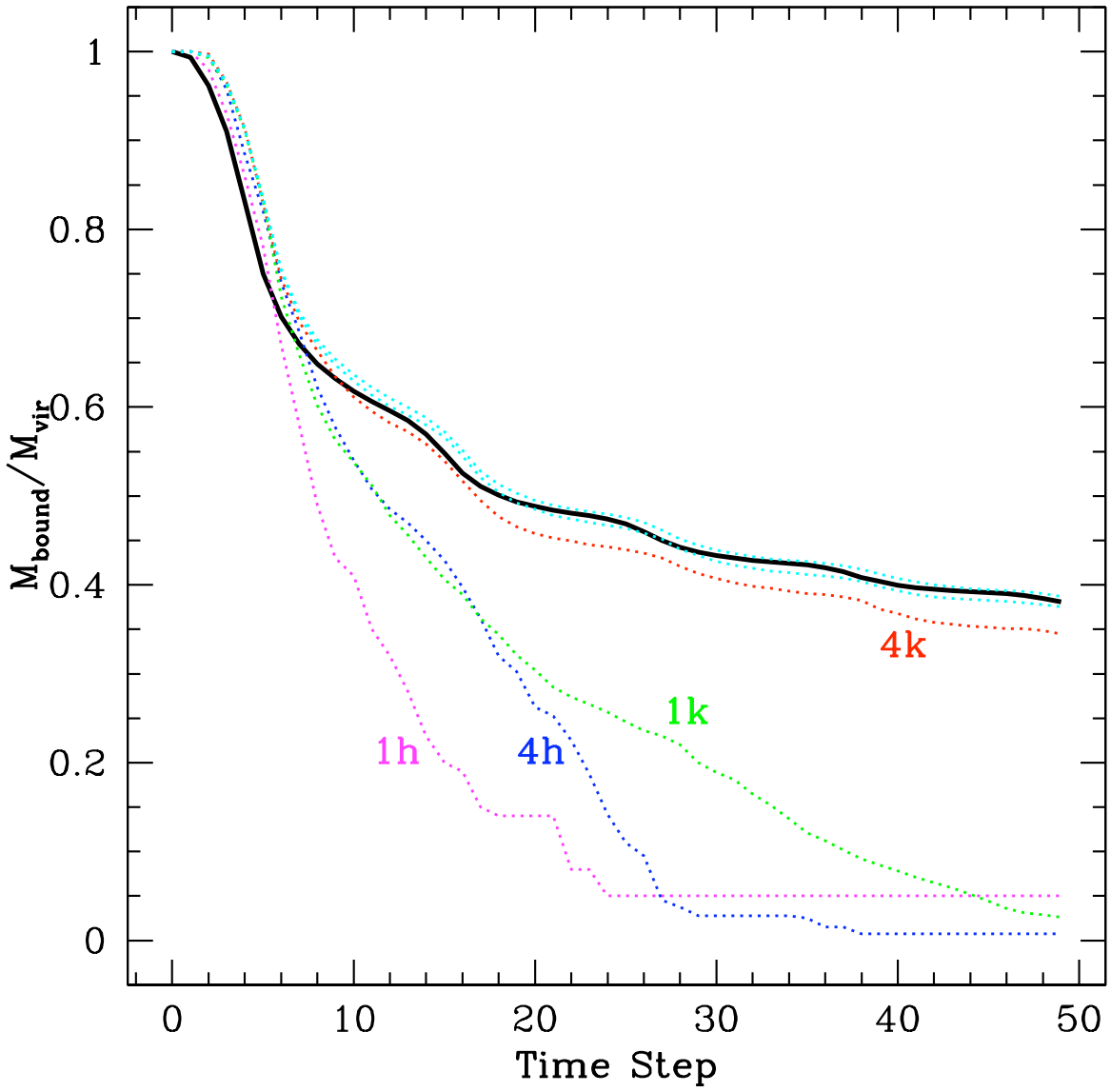

Figure 5.2: Mass Loss for Different Resolutions. The black solid curve is the mass loss in the highest resolution 100k. The dotted curves show mass loss for lower resolutions. Mass loss in resolutions 10k and 40k (cyan curves) are similar to 100k.

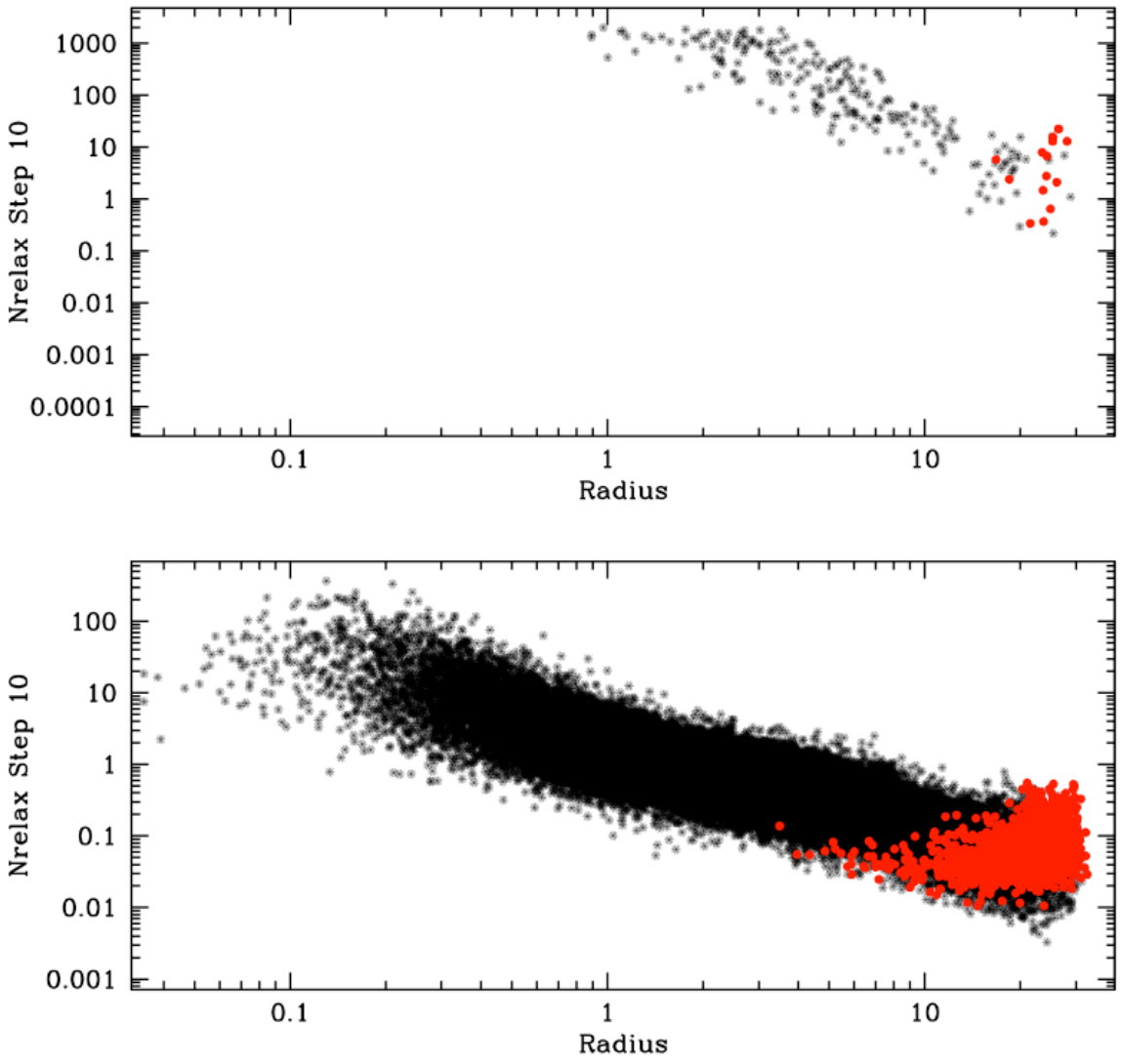

Figure 5.3: N_{relax} versus Radius for Resolutions 4h (top) and 100k (bottom). N_{relax} is the number of crossings for the energy of each particle in the simulation to change by of order itself. It has been calculated for each bound particle (black points) at the 10th time step of the simulation. The red points are N_{relax} for the particles that have got unbound in that particular time step. We see that in the high resolution simulation (bottom) the particles getting unbound have less than one relaxation crossing whereas the particles getting unbound in the lower resolution simulation (top) have more than one relaxation crossing.

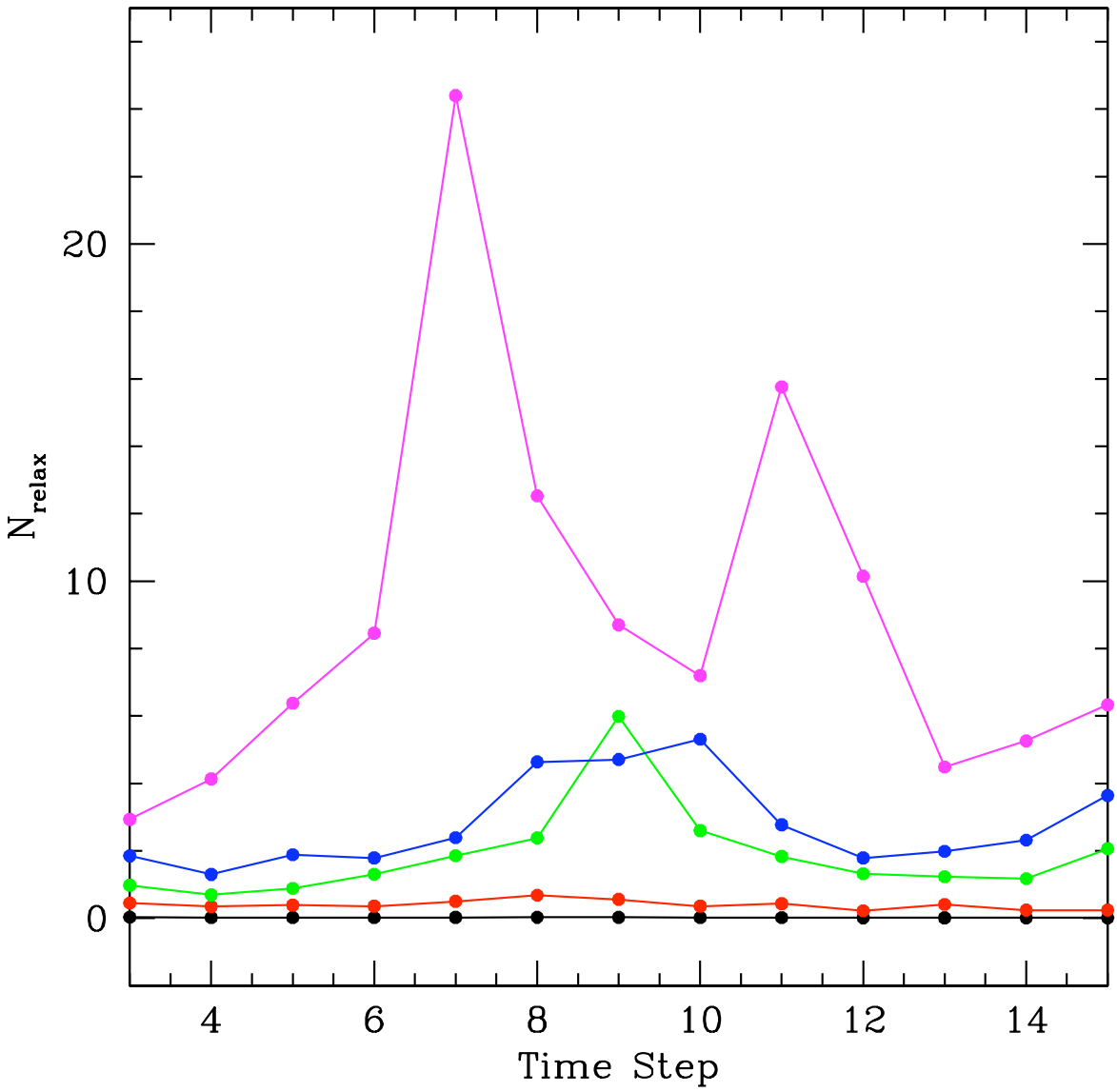

Figure 5.4: Average number of relaxation crossings of unbound particles versus time step for different resolutions. From bottom to top the resolutions are 100k (black), 4k (red), 1k (green), 4h (blue) and 1h (magenta). The resolutions 40k and 10k are similar to 100k (black). The average number of relaxation crossings is calculated over particles getting unbound in that particular time step of the simulation (the red points in figure 5.3).

Chapter 6

Conclusion

The purpose of cosmology as any other field of science is to ask questions, make predictions and test those predictions with experiments. The process is usually inverted when new observations challenge existing theories and incite cosmologists to come up with new theoretical models. However there is a gap between mathematical models of the universe that are usually based on simple assumptions and the complicated, almost chaotic data from astrophysical observations. This gap is filled by cosmological simulations. The input of these simulations is provided by the cosmological model. It forms the initial conditions of the simulation. The output is the prediction of the current state of the universe, in other words the mass, shape and distribution of current structures that can be compared with observations. These predictions tested with observational data may confirm or refute the model used for the simulation. For instance a simulation that starts with Gaussian fluctuations in the density of matter predicted by inflationary models of cosmology and assumes dark matter to be cold would make predictions that are different from a simulation that assumes a non-Gaussian field or in which dark matter is warm. As the fate of models lies in the hands of simulations, the latter need to be reliable.

Purely gravitational simulations, in other words those in which we do not need to take into account the complicated processes of baryons, mainly suffer from numerical limitations. The simulations including baryons lack the necessary physics in addition to numerical problems. The physics of a purely gravitational system is well-understood, however limited

dynamic range, force accuracy and time integration accuracy of the simulation are issues that need to be taken account. Among these, dynamic range has long been considered as the most severe problem, specially when the total resolution of the simulations was of the order $N = 10^5$ (before the 90s). Since then, the resolutions of cosmological simulations have increased exponentially with the advance of computing technology reaching about $N = 10^{10}$ today. However even in these simulations the smallest structures have less than 100 particles where the mass of individual particles is about 10^{10} solar masses. For instance in the simulations of Springel et al. (2005) the smallest subhalos had about 20 particles. We saw from our relaxation analysis in the last section that when satellites have this number of particles they are affected by artificial effects that might cause their disruption or at least the underestimation of their mass. Therefore the outcome of cosmological simulations in small scales may not be reliable. In this case an analytic model predicting the evolution of substructure can test the reliability of cosmological simulations in different scales and make an alternative prediction when simulations suffer from lack of resolution. In addition such a model is much less computationally expensive than the cosmological simulations, making it an attractive alternative.

In addition, cosmological simulations are far from having the necessary resolution for studying dark matter in small scales such as the scale of the solar system. The minihalos on these scales have masses of $\simeq 10^{-6}\ M_\odot$ and the number of particles needed to resolve them in cosmic simulations is of order 10^{20}. If the technological advances in computational power continue growing exponentially we will need another 50 years to reach this resolution. Therefore it is necessary to analytically predict how small halos are distributed and how dense they are locally. This in turn affects the calculated annihilation rate of dark matter particles and guides us in our attempts to detect the dark matter particle. Thus we definitely need analytic models describing the evolution of subhalos and their mass loss in minor mergers.

The analytic tidal model explained in chapter 3 describes the evolution of substructure with high accuracy taking into account a few physical phenomena. These phenomena had been individually studied before in other astrophysical contexts such as globular cluster interactions with the galaxy. But it was first Taylor & Babul (2001) who developed a simple

analytic model incorporating them altogether for the study of substructure dynamics. This simple model takes into account two major processes in order to describe tidal interactions: The first is tidal truncation due to the tidal field of the host unbinding particles at a tidal limit where the gravitational field of the host becomes stronger than the gravitational field of the satellite. This is a steady-state approximation as it assumes that the structure of the satellite isn't changed due to the tidal field. This truncation scheme should be coupled with a heating calculation that finds the amount of energy change at pericentral passages due to tidal shocks and corrects the tidal radius at pericenter. To also take into account the higher moments of energy change and the virialization of the satellite, the energy change was multiplied by a factor ϵ_h. Taylor & Babul (2001) also took into account the dynamical friction from the host halo and calibrated their model to fit simulation data.

As there were discrepancies between the model predictions and the data, we isolated tidal interactions ignoring dynamical friction by having a static host and studied the mass loss of the satellite following the main guidelines of the Taylor & Babul (2001) (TB01) approach. Our first important conclusion is that the mass lost beyond the tidal limit of the satellite should be scaled as it takes time for particles to be effectively separated from the satellite. Our scaling was half the instantaneous orbital period of the satellite, which differs from the TB01 approach as they chose one orbital period. We calibrated the heating of the satellite using the actual energy change of particles in the simulation which was not possible in TB01 as other processes were involved other than heating. Thus TB01 calibrated their final results comparing the mass loss predicted by the model with the actual mass loss of the satellite. Here the direct comparison with the energy change gave us a more accurate value of the heating parameter $\epsilon_h = 3.4$ which was higher than the TB01 value $\epsilon_h = 3.0$. However it is still closer to TB01 than to Gnedin & Ostriker (1999) as the latter had used $\epsilon_h = 7/3$.

We find our new tidal radii based on the change of energy from shocks. TB01 assumed that the structure of the satellite does not change in their derivation of the change in the average density from heating. We calculate the change in the average density in each time step in a similar way. Which means we calculate the effect of shocks close to pericenter and neglect them everywhere else. The change in the average density is *cumulative*. This means

that the $\Delta\bar{\rho}_{tot}$ used to calculate the tidal radii in each time step has in itself the $\Delta\bar{\rho}$ of that time step plus all the contributions of the previous time steps. The new set of tidal radii found this way (r_m in chapter 4) are different from the tidal radii found without taking heating into account (r_t), in the sense they do not oscillate between fixed values but rather decrease while slightly oscillating between pericenter and apocenter. We find that the density of the satellite really changes as it expands because of heating and the effect of this change is present in the subsequent steps of the satellite's evolution. Thus the tidal radii decrease with time as the satellite is expanding and the equality of the gravitational fields of the host and satellite (the tidal limit) happens more toward the center of the expanded satellite. This approach in calculating tidal radii has two remarkable implications.

First, if the new tidal radii are used to truncate an NFW density profile they result in a very accurate prediction of mass loss. This accuracy can not be directly compared to the accuracy of TB01 mass loss curves as other phenomena are taken into account there such as dynamical friction, galactic disk, bulge,... The second implication of this new set of tidal radii is that they give us the only parameter needed to describe the updated density profile of the satellite. The new density profile of the expanded satellite is modified by a factor which is a function of radius and is given having r_m. This result is an analytic prediction of substructure density evolution while Hayashi et al. (2003) and others have used fits to numerical results to find a similar behavior for the density evolution. The new density profile is close to NFW up to about $r = 0.4\ r_m$ and diverges from it afterwards. This difference is more pronounced at $r = r_m$. After that the satellite's density decreases rapidly in a way that results in a cut-off in the mass of the satellite. The bound mass of the satellite will be equal to the NFW mass enclosed in r_m. This is why truncating an NFW profile at this tidal radius gives a correct mass loss. Although the set of tidal radii are smaller than the previously calculated tidal radii r_t for which we didn't take into account the effect of heating, the bound particles are not limited to r_m and some particles lie between r_m and r_t. This is because the tidal limit of the satellite is not well defined when we are not in the steady-state regime and have expansion. The outer limit of the satellite is given by r_t. The high accuracy of the tidal model and its cost efficiency compared to cosmological simulations make it an excellent alternative for studying the evolution of substructures and their tidal interactions with dark matter halos that host them.

References

Begeman, K. G., Broeils, A. H., & Sanders, R. H. 1991, Monthly Notices of the Royal Astronomical Society, 249, 523 5

Benson, A. J. 2010, ArXiv Astrophysics e-prints 10

Bertone, G., Hooper, D., & Silk, J. 2005, Physics Reports, 405, 279

Bertschinger, E. 2001, The Astrophysical Journal Supplement Series, 137, 1 11

Binney, J. & Tremaine, S. 1994, Galactic Dynamics (Princeton, New Jersey 08540: Princeton University Press) 18, 20, 24, 25, 27, 32, 45, 66, 82

Blumenthal, G., Faber, S., Primack, J., & Rees, M. 1984, Nature, 311, 517 6

Diemand, J., Moore, B., & Stadel, J. 2005, Nature, 433, 389 12

Diemand, J., Moore, B., Stadel, J., & Kazantzidis, S. 2004, Monthly Notices of the Royal Astronomical Society, 348, 977 66, 67

Eddington, A. S. 1916, Monthly Notices of the Royal Astronomical Society, 76, 572 20

Frenk, C. S. 2002, Royal Society of London Philosophical Transactions Series A, 360, 1277 4

Gnedin, O. Y. & Ostriker, J. P. 1997, The Astrophysical Journal, 474, 223 52

—. 1999, The Astrophysical Journal, 513, 626 45, 51, 74

Green, A. M. & Goodwin, S. P. 2007, Monthly Notices of the Royal Astronomical Society, 375, 1111 12, 14

Green, A. M., Hofmann, S., & Schwarz, D. J. 2004, Monthly Notices of the Royal Astronomical Society, 353, L23 7

Hayashi, E., Navarro, J. F., Taylor, J. E., Stadel, J., & Quinn, T. 2003, The Astrophysical Journal, 584, 541 13, 59, 60, 61, 75

Hernquist, L. 1993, The Astrophysical Journal Supplement Series, 86, 389 21

Innanen, K. A., Harris, W. E., & Webbink, R. F. 1983, Astronomical Journal, 88, 338

Kazantzidis, S., Magorrian, J., & Moore, B. 2004a, The Astrophysical Journal, 601, 37 17, 22

Kazantzidis, S., Mayer, L., Mastropietro, C., Diemand, J., Stadel, J., & Moore, B. 2004b, The Astrophysical Journal, 608, 663 13, 61

King, I. 1962, The Astrophysical Journal, 67, 471 36

Klypin, A., Gottlöber, S., Kravtsov, A. V., & Khokhlov, A. M. 1999, The Astrophysical Journal, 516, 530 11

Kundic, T. & Ostriker, J. P. 1995, The Astrophysical Journal, 438, 702 44

Mamon, G. 1993, in N-body Problems and Gravitational Dynamics, ed. F. Combes & E. Athanassoula, 188–203

Mamon, G. A. 1987, The Astrophysical Journal, 321, 622

Mellier, Y. & van Waerbeke, L. 2001, ArXiv Astrophysics e-prints 6

Merritt, D. 1985, Astronomical Journal, 90, 1027

Moore, B., Ghigna, S., Governato, F., Lake, G., Quinn, T., Stadel, J., & Tozzi, P. 1999, The Astrophysical Journal, 524, L19 11

Navarro, J. F., Frenk, C. S., & White, S. D. M. 1996, The Astrophysical Journal, 462, 563 9, 17

Navarro, J. F., Hayashi, E., Power, C., Jenkins, A. R., Frenk, C. S., White, S. D. M., Springel, V., Stadel, J., & Quinn, T. R. 2004, Monthly Notices of the Royal Astronomical Society, 349, 1039 10

Osipkov, L. P. 1979, Pis ma Astronomicheskii Zhurnal, 5, 77

Ostriker, J. P., Spitzer, Jr., L., & Chevalier, R. A. 1972, The Astrophysical Journal, 176, L51 41

Ostriker, J. P. & Steinhardt, P. J. 1995, ArXiv Astrophysics e-prints

Padmanabhan, T. 1993, Structure Formation in the Universe (Cambridge, UK CB2 1RP: Cambridge University Press) 8

Perlmutter, S., Aldering, G., Goldhaber, G., Knop, R. A., Nugent, P., Castro, P. G., Deustua, S., Fabbro, S., Goobar, A., Groom, D. E., Hook, I. M., Kim, A. G., Kim, M. Y., Lee, J. C., Nunes, N. J., Pain, R., Pennypacker, C. R., Quimby, R., Lidman, C., Ellis, R. S., Irwin, M., McMahon, R. G., Ruiz-Lapuente, P., Walton, N., Schaefer, B., Boyle, B. J., Filippenko, A. V., Matheson, T., Fruchter, A. S., Panagia, N., Newberg, H. J. M., Couch, W. J., & The Supernova Cosmology Project. 1999, The Astrophysical Journal, 517, 565 6

Press, W. H. & Schechter, P. 1974, The Astrophysical Journal, 187, 425 8

Ryden, B. 2003, Introduction to Cosmology (San Francisco, CA 94111: Addison Wesley) 3

Spergel, D. N., Verde, L., Peiris, H. V., Komatsu, E., Nolta, M. R., Bennett, C. L., Halpern, M., Hinshaw, G., Jarosik, N., Kogut, A., Limon, M., Meyer, S. S., Page, L., Tucker, G. S., Weiland, J. L., Wollack, E., & Wright, E. L. 2003, The Astrophysical Journal, 148, 175 7

Spitzer, Jr., L. 1958, The Astrophysical Journal, 127, 17 41, 45

Springel, V. & White, S. D. M. 1999, Monthly Notices of the Royal Astronomical Society, 307, 162 17

Springel, V., White, S. D. M., Jenkins, A., Frenk, C. S., Yoshida, N., Gao, L., Navarro, J., Thacker, R., Croton, D., Helly, J., Peacock, J. A., Cole, S., Thomas, P., Couchman, H., Evrard, A., Colberg, J., & Pearce, F. 2005, Nature, 435, 629 9, 15, 73

Springel, V., Yoshida, N., & White, S. D. M. 2001, New Astronomy, 6, 79 22, 24

Taylor, J. & Babul, A. 2001, The Astrophysical Journal, 559, 716 13, 14, 36, 38, 42, 44, 51, 52, 73, 74

Tormen, G., Diaferio, A., & Syer, D. 1998, Monthly Notices of the Royal Astronomical Society, 299, 728 26

Tytler, D., O'Meara, J. M., Suzuki, N., & Lubin, D. 2000, Physics Reports, 333, 409 4

Velazquez, H. & White, S. D. M. 1999, Monthly Notices of the Royal Astronomical Society, 304, 254 13

von Hoerner, S. 1957, The Astrophysical Journal, 125, 451 32, 33

Weinberg, M. D. 1994, The Astronomical Journal, 108, 1398 45

White, S. D. M. & Rees, M. J. 1978, Monthly Notices of the Royal Astronomical Society, 183, 341

APPENDICES

Appendix A

Orbital Periods

As mentioned in the second chapter the integrals of motion in a spherical potential are:

(1) The angular moemntum: $L = r^2\dot{\psi}$.

(2) The energy: $E = \frac{1}{2}\dot{r}^2 + \frac{1}{2}(r\dot{\psi})^2 + \phi(r)$.

Where r is the distance to center of the potential and ψ is the azimuthal angle. From the definition of the energy, we can write:

$$\frac{dr}{dt} = \pm\sqrt{2[E - \Phi(r)] - \frac{L^2}{r^2}} \tag{A.1}$$

The two radii r_1 and r_2 at which the above equation goes to zero are the apocenter and pericenter distances of the orbit. The **radial period** is defined as the time it takes to go from r_1 to r_2 and then to r_1 again:

$$T_r = 2\int_{r_1}^{r_2} \frac{dr}{\sqrt{2[E - \Phi(r)] - L^2/r^2}} \tag{A.2}$$

In traveling from pericenter to apocenter and back the azimuthal angle changes by the amount:

$$\Delta\psi = 2\int_{r_1}^{r_2} \frac{d\psi}{dr}dr = 2\int_{r_1}^{r_2} \frac{L}{r^2}\frac{dt}{dr}dr \tag{A.3}$$

Substituting for dt/dr from equation A.1 we get:

$$\Delta\psi = 2L\int_{r_1}^{r_2} \frac{dr}{r^2\sqrt{2[E - \Phi(r)] - L^2/r^2}} \tag{A.4}$$

The **azimuthal period** is defined as:

$$T_\psi = (2\pi/\Delta\psi) \times T_r \tag{A.5}$$

For more details on orbital dynamics see Binney & Tremaine (1994).

Appendix B

Tidal Acceleration Terms

We saw in chapter 3 that the X component of the tidal acceleration at the center of mass of the satellite is given by:

$$\mathbf{g}_X = -\frac{GM_{vir}}{\ln(1+c) - c/(1+c)} \frac{\ln(1+R/r_s) - R/(r_s+R)}{R^3} X \tag{B.1}$$

Where $R = \sqrt{X^2+Y^2+Z^2}$ is the position of the center of mass of the satellite, r_s is the scale radius of the satellite, M_{vir} is the virial mass of the satellite and c is the satellite's concentration. We want to find $\partial g_X/\partial X$, $\partial g_X/\partial Y$ and $\partial g_X/\partial Z$. We rewrite B.1 as:

$$\mathbf{g}_X = A \times B(R) \times C(X) \tag{B.2}$$

$$A = -\frac{GM_{vir}}{\ln(1+c) - c/(1+c)} \tag{B.3}$$

$$B(R) = \ln(1+R/r_s) - R/(r_s+R) \tag{B.4}$$

$$C(X) = \frac{X}{R^3} \tag{B.5}$$

$$\partial g_X/\partial X = A\left[\frac{\partial B}{\partial X} C + \frac{\partial C}{\partial X} B\right] \tag{B.6}$$

$$\frac{\partial B}{\partial X} = \frac{\partial B}{\partial R}\ \frac{\partial R}{\partial X} = \frac{R + r_s - r_s^3}{(r_s + R)^2}\ \frac{X}{R} \tag{B.7}$$

$$\frac{\partial C}{\partial X} = \frac{\partial C}{\partial R}\ \frac{\partial R}{\partial X} = \frac{R^2 - 3X^2}{R^5} \tag{B.8}$$

Therefore from B.6:

$$\partial g_X/\partial X = -\frac{GM_{vir}}{\ln(1+c) - c/(1+c)}\ \frac{R + r_s - r_s^3}{(r_s + R)^2}\ \frac{X^2}{R^4} + \frac{R^2 - 3X^2}{R^5}\ \Big[\ln(1 + R/r_s) - R/(r_s + R)\Big] \tag{B.9}$$

Similarly:

$$\partial g_X/\partial Y = -\frac{GM_{vir}}{\ln(1+c) - c/(1+c)}\ \frac{R + r_s - r_s^3}{(r_s + R)^2}\ \frac{XY}{R^4} - \frac{3XY}{R^5}\ \Big[\ln(1 + R/r_s) - R/(r_s + R)\Big] \tag{B.10}$$

$$\partial g_X/\partial Z = -\frac{GM_{vir}}{\ln(1+c) - c/(1+c)}\ \frac{R + r_s - r_s^3}{(r_s + R)^2}\ \frac{XZ}{R^4} - \frac{3XZ}{R^5}\ \Big[\ln(1 + R/r_s) - R/(r_s + R)\Big] \tag{B.11}$$

$$\partial g_Y/\partial X = -\frac{GM_{vir}}{\ln(1+c) - c/(1+c)}\ \frac{R + r_s - r_s^3}{(r_s + R)^2}\ \frac{YX}{R^4} - \frac{3YX}{R^5}\ \Big[\ln(1 + R/r_s) - R/(r_s + R)\Big] \tag{B.12}$$

$$\partial g_Y/\partial Y = -\frac{GM_{vir}}{\ln(1+c) - c/(1+c)}\ \frac{R + r_s - r_s^3}{(r_s + R)^2}\ \frac{Y^2}{R^4} + \frac{R^2 - 3Y^2}{R^5}\ \Big[\ln(1 + R/r_s) - R/(r_s + R)\Big] \tag{B.13}$$

$$\partial g_Y/\partial Z = -\frac{GM_{vir}}{\ln(1+c) - c/(1+c)}\ \frac{R + r_s - r_s^3}{(r_s + R)^2}\ \frac{YZ}{R^4} - \frac{3YZ}{R^5}\ \Big[\ln(1 + R/r_s) - R/(r_s + R)\Big] \tag{B.14}$$

$$\partial g_Z/\partial X = -\frac{GM_{vir}}{\ln(1+c) - c/(1+c)}\ \frac{R + r_s - r_s^3}{(r_s + R)^2}\ \frac{ZX}{R^4} - \frac{3ZX}{R^5}\ \Big[\ln(1 + R/r_s) - R/(r_s + R)\Big] \tag{B.15}$$

$$\partial g_Z/\partial Y = -\frac{GM_{vir}}{\ln(1+c)-c/(1+c)}\,\frac{R+r_s-r_s^3}{(r_s+R)^2}\,\frac{ZY}{R^4}-\frac{3ZY}{R^5}\,\Big[\ln(1+R/r_s)-R/(r_s+R)\Big] \tag{B.16}$$

$$\partial g_Z/\partial Z = -\frac{GM_{vir}}{\ln(1+c)-c/(1+c)}\,\frac{R+r_s-r_s^3}{(r_s+R)^2}\,\frac{Z^2}{R^4}+\frac{R^2-3Z^2}{R^5}\,\Big[\ln(1+R/r_s)-R/(r_s+R)\Big] \tag{B.17}$$

We have nine terms for the $g_{a,b} = \partial g_a/\partial X_b$. Substituting these terms in equation 3.29 will give use the tidal acceleration of particles in the satellite.